AIAA-2026-1506

REGULATION OF THE AERODYNAMIC LOADS ON A CIRCULAR CYLINDER USING 2- AND 3-D COANDA WALL JET ARRAYS

Nathan Rackers, Michael DeSalvo, Bojan Vukasinovic and Ari Glezer
Georgia Institute of Technology, Atlanta GA USA

Abstract

Aerodynamic loads engendered by circulation control on a rotorcraft cylinder boom have been used to effect counter torque to replace the conventional tail rotor in NOTAR configurations. These loads that have been realized by the Coanda effect of a 2-D steady wall jet in the rotor downwash diminish with changes in the direction of the cross flow in sideward and forward flight and are typically augmented by an additional jet thruster. The present wind tunnel investigations explore the utility of segmented Coanda actuation on a circular cylinder model for generating streamwise and cross-stream loads that are less insensitive to the direction of the cross flow using spanwise arrays of 3-D fluidically oscillating wall jets with specific emphasis on the interaction of the control jets with the cross flow and their effects on the near wake. It is shown that for a common actuation momentum coefficient (and at a lower actuation power) the 3-D jets lead to markedly higher cross-stream loading than the 2-D jets and an extended azimuthal range of effective actuator positions. The lift increments of the 2- and 3-D jets are also accompanied by drag decrements of up to ~40%. The present investigations are conducted at subcritical Reynolds number ($Re_D = 2.1 \cdot 10^5$) and the effects of supercritical flow on the interaction of the 3-D jets with the cross flow were assessed by tripping the boundary layer upstream of the azimuthal position of the jet and taking load measurements coupled with planar PIV. When the actuation is applied upstream of its critical (highest lift) azimuthal position, the state of the boundary layer has minimal effect on the induced aerodynamic loads. However, near the critical actuation angle over the smooth cylinder perturbations in the tripped upstream boundary layer can strongly disrupt the interactions of the jets with the cross flow and significantly reduce the effected lift. These effects are investigated in the absence and presence of tripping using POD analysis of instantaneous PIV data.

I. INTRODUCTION

Conventional tail rotors have been used to produce the counter torque needed for operation of single rotor helicopters since they were developed and flown in the late 1930s (Sikorsky 1942). However, over the years it has been recognized that the tail rotor poses a number of operational disadvantages including mechanical complexity and weight, significant power loss, added noise, risk of loss of directional control by striking structures, and danger to ground crews (Klemin 1948). Early endeavors to replace the tail rotor focused on the use the thrust of integrated exhaust air jets for direct control of the torque (e.g. McDaniel 1961).

The NOTAR (No Tail Rotor) system was developed in the 1970s to produce sufficient counter torque to replace the conventional tail rotor by leveraging circulation control using the Coanda effect resulting from interaction of the main rotor downwash with a nominally two-dimensional wall jet issuing tangentially on a segment of the tail boom (Hanvey 1982; Sampatacos et al. 1983; Logan and Kumar 1986). To improve yaw control authority (particularly in forward flight), the wall-jet was augmented with a vectored jet nozzle at the end of the tail boom and a vertical tail. Flight tests of an OH-6A helicopter equipped with the NOTAR system (Hanvey 1982) demonstrated that circulation control can become less effective in rearward and sideward flight and even more so in forward flight requiring larger thrust from the direct jet where in forward flight the majority of yaw control is provided by the vertical tail and by the thrust jet. These flight tests demonstrated that the overall NOTAR system is flightworthy and leads to improved hover stability and reduced noise and vibration and while noted that shortcomings in lateral-directional flying qualities at high speed could be eliminated through design modifications. More recently, Luo et al. (2000) assessed the aerodynamic characteristics of a NOTAR helicopter tail boom in a wind tunnel test, finding that the effectiveness of the circulation control component of the system was improved by about 15% by using two jet slots on the same side of the tail boom. Dionisio and Nurick (2001) performed wind tunnel tests of a circular cylinder in a cross flow with two wall jets and assessed the relative contributions to lift and drag of the free stream flow and the wall jets. In a related work, Nurick (2001) tested a circular cylindrical tail boom (terminating in a flat circular surface) in the wake of a rotor and developed a method for predicting the torque of the tail boom using results using two-dimensional wind tunnel data

The Coanda effect exhibited in the NOTAR system has been the subject of numerous earlier investigations over cylinders. The evolution of an isolated 2-D turbulent wall jet issuing tangentially over the surface of a cylinder in the absence of a cross flow was first analyzed by in a seminal paper by Newman (1961) who characterized the deflection of the jet along the surface owing to the Coanda effect including the changes in distribution of its cross stream velocity and the surface pressure and the separation of the jet from the surface. Newman also compared wall jets around the cylinder to similar jets along a flat plane and an inclined plane. In an experimental investigation, Neuendorf and Wygnanski (1999) characterized the evolution of a wall jet over a circular cylinder and identified the conditions under which separation occurs compared to a flat plane wall jet. Subsequently, Neuendorf et al. (2004) characterized the streamwise vortices within the turbulent wall jet that are formed on the convex surface due to a centrifugal instability and identified the presence of counter-rotating vortex pairs that migrate along the cylinder axis and were believed to affect separation of the jet from the surface.

In the presence of a cross flow, the Coanda effect over a circular cylinder becomes more prominent, when streamwise flow attachment over one side of the cylinder is increased resulting in flow asymmetry over the cylinder and in a large force (normal to the cross flow direction) that is accompanied by change in the azimuthal position of the front and rear stagnation points and circumferential circulation. Lockwood (1960) reported that a wall jet having momentum coefficient $C_\mu = 0.15$ leads to a normal force of $C_N = 3$, and that larger forces can be realized using multiple tangential jets at successive azimuthal positions. In another remarkable work, Dunham (1968) developed a model based on boundary layer theory and potential flow formulation to estimate the location of separation for a given free stream Re, C_μ, slot width and azimuthal position, from which the resulting C_N was estimated with good agreement with prior experiments. In a similar comparison between experiments and a model based on potential flow and boundary layer theory, Levinsky and Yeh (1972) showed that for a given C_μ, C_N is influenced by the jet azimuthal position θ, with maximum C_N for $\theta \sim 110°$. The effect of the wall jet on the drag of the cylinder C_D was studied by

Oh and Roberts (1989) who used a discrete vortex model to show up to 4-fold reduction in drag at $C_\mu = 0.1$. The effects of jet angular position θ and slot width were investigated by Williams and Cummings (1996, $Re = 1.3 \cdot 10^5$) who showed that jets located immediately upstream of separation were most effective at increasing C_N, and that reduction of the slot width enabled the same C_N to be achieved with reduced mass flow. In a combined set of experiments ($Re = 1.1 \cdot 10^5$ and $1.7 \cdot 10^5$) and RANS numerical simulations, Runge et al. (2015) characterized the pressure distributions and corresponding C_N and C_D on the cylinder, finding good agreement between experiments and simulations. Streamlines from the simulations clearly show the flow asymmetry relative to the direction of the cross flow and the changes in the locations of the front and rear stagnation points. The aerodynamic effects of an *unsteady*, time-periodic 2-D wall jet over a circular cylinder ($Re = 1.9 \cdot 10^5$) were investigated by Ghee and Leishman (1992), who found that for reduced frequencies $k \leq 0.2$, the mean C_N increased by about 20%-50% compared to steady actuation at the same C_μ, with a slight reduction in C_D.

Circulation control over aircraft wings by using nominally 2-D surface wall jets and the Coanda effect on lifting and the control surfaces can effect remarkable changes in aerodynamic performance and has been known since the 1930s (e.g. Metral, 1939). Such Coanda-based circulation control has been investigated extensively, perhaps most notably by Englar and his co-workers (e.g., 2000, 2003). While the earlier work has utilized almost exclusively 2-D wall jets, recent circulation control investigations (Vukasinovic et al., 2025) demonstrated the utility of arrays of unsteady, 3-D fluidically-oscillating wall jets. The present wind tunnel investigations focus on and explore the potential use of 3-D jets for circulation control to manage the NOTAR counter torque by the induced aero-effected loads on the boom cylinder that have been traditionally realized by 2-D steady wall jets. The present work focuses on characterization and comparison of the aerodynamic effects of 2-D wall jets and a spanwise arrays of 3-D of equally-spaced fluidically oscillating jets in transitional flow over a smooth circular cylinder at subcritical Reynolds numbers (§III). The effects of a turbulent boundary layer mimicked by a surface trip on the aerodynamic loads induced by the 3-D jets on the cylinder are discussed in §IV.

II. EXPERIMENTAL SETUP AND FLOW DIAGNOSTICS

The present wind tunnel investigations of circulation control are conducted using a circular cylinder model of diameter $D = 152$ mm and span $S = 885$ mm (Figure 1a) comprising five spanwise segments of equal length where each segment can accommodate interchangeable modules of either a 2- or 3-D Coanda wall jets. The model is mounted on two 6-component load cells on either side of the wind tunnel's square test section (91.4 cm on the side) having a maximum speed of 35 m/s. The azimuthal coordinate over the surface of the cylinder θ and azimuthal position of the jet array α (adjusted by rotating the model about its axis) are measured relative to the upstream intersection of the surface with a reference line through the cylinder's center aligned with the direction of the free stream. The vertical and horizontal loads L and D model the rotorcraft tail boom side force and download, respectively (Figure 1b). The present experiments are performed primarily at a free stream speed of $U_0 = 25$ m/s at a subcritical $Re_D = 2.1 \cdot 10^5$.

The 2- and 3-D wall jet modules that are assembled into each of the cylinder's segments are fabricated using stereolithography and each jet module has a dedicated separate plenum that connects to a central air supply through the model's spar. Both the 2- and 3-D wall jets issue from underneath an overhang tangentially to a shallow recess in the surface that blends into the outer circular surface within nominally 25 jet heights downstream. It is noted that while the height of the 2-D Coanda jet for optimal lift generation on a circular trailing edge of a circulation control wing was $h = 0.01D$ (Englar and Blaylock, 2010), the lift produced at $h = 0.005D$ was only about 8% lower. The height of the present 2-D jet orifices (Figures 1c and e) was selected to be somewhat lower ($0.003D$, 0.46 mm) to yield a range of actuation momentum coefficients that have a reasonable overlap with the momentum coefficient of the 3-D jets as discussed further below. To this end, the overhang of the 2-D wall jet modules was fabricated using steel plate as shown in Figure 1e. The 3-D jet array module (Figures 1d) includes seven discrete, equally-spaced (24.8 mm, $0.16D$ apart) jets in each spanwise segment oscillating in the spanwise direction at a nominal frequency of 3-4 kHz (flow rate dependent) with orifices that are 1.52 mm high and 1.26 mm wide (Figure 1f). Each of the jets in the 3-D module can be blocked off from the module's plenum to enable different groupings of the actuation jets. In the present investigations, arrays with spanwise jet spacings of $0.16D$, $0.33D$, $0.49D$ and $1.14D$ across the span were tested. In the $0.04D$ space between any pair of spanwise segments, the model can be equipped with azimuthal disc inserts each including 27 azimuthally distributed static pressure ports for measurement of azimuthal pressure distribution around the cylinder. The flow at the exit plane of the 2- and 3-D actuator jet modules was surveyed $0.087D$ downstream of the jet exit plane using a miniature total pressure probe to estimate the velocity normal to the exit plane u_t in the absence of cross flow (Figure 2). The 2-D jet (Figure 2a) is relatively uniform across the model span, with variations within ±5%. The variations in the peak velocity of the 3-D jets (Figure 2b) ±9% is attributed to slight variations in the SLA fabrication.

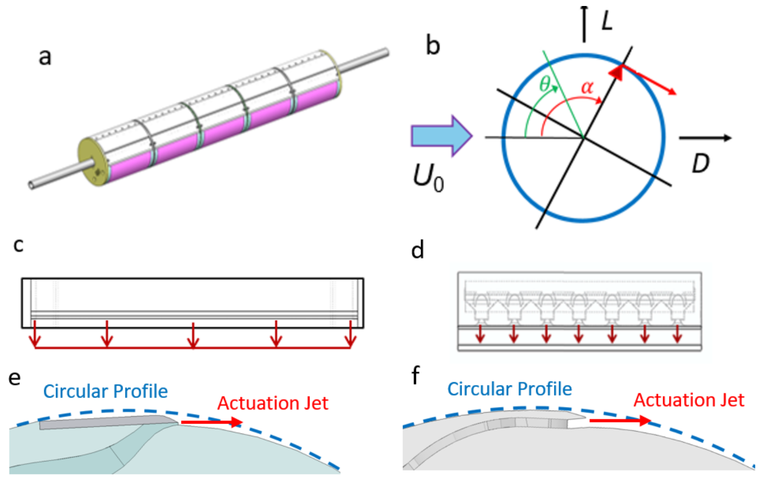

Figure 1. *a) The spanwise-segmented circular cylinder wind tunnel model, b) Schematic of the model cross section, Top views of the c) 2-D wall jet actuator module, and d) 3-D wall fluidically-oscillating wall jet actuator array, The orifice configurations of the (e) 2-D actuator, and (f) 3-D actuator.*

The actuation jet momentum is characterized by measuring the jet thrust force ***T*** *in situ* on the cylinder model for a range of mass flow rates in the absence of cross flow. Figure 3 shows the variation of the jet (force based, Vukasinovic, Funk, and Glezer, 2025) momentum coefficient $C_\mu^F = T/(\frac{1}{2}\rho U_o{}^2 DL)$ with the scaled mass flow rate $C_Q = \dot{m}/(\rho U_o DL)$ for $U_o = 25$ m/s. These data were measured for the 2-D jets and for different spacings of the 3-D jets (0.16, 0.33, 0.49, and 1.14D apart) up to $C_\mu^F = 0.15$. It is remarkable that despite the interactions with the surface of the

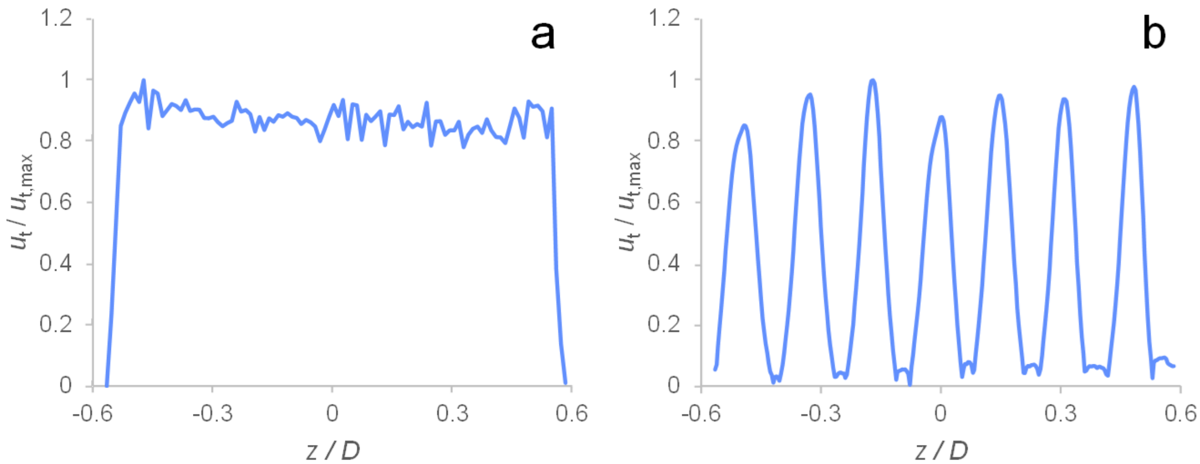

Figure 2. *Spanwise variation of the speed estimated from total pressure measurements 0.087D downstream of the 2- and 3-D (a and b, respectively) actuator jet exit planes. The measured velocity is scaled by the maximum local jet velocity $u_{t,max}$.*

cylinder C_μ^F varied approximately linearly with $(C_Q)^2$. It should be noted that because the total orifice area of the 2-D jet is about 5 times larger than that of even the densest array of 3-D jets, the C_Q required to effect a given C_μ^F is significantly higher for the 2-D jets. For the 3-D jets, the highest thrust for a given mass flow is achieved using jets spaced every 1.14D ($N_j = 5$). However, as seen in Figure 3, the maximum effected C_μ^F increases with N_j since the maximum C_Q per jet was kept constant for different jet arrays. In the case of the 2-D jet, the realized range of C_μ^F is limited by mass flow rate constraints.

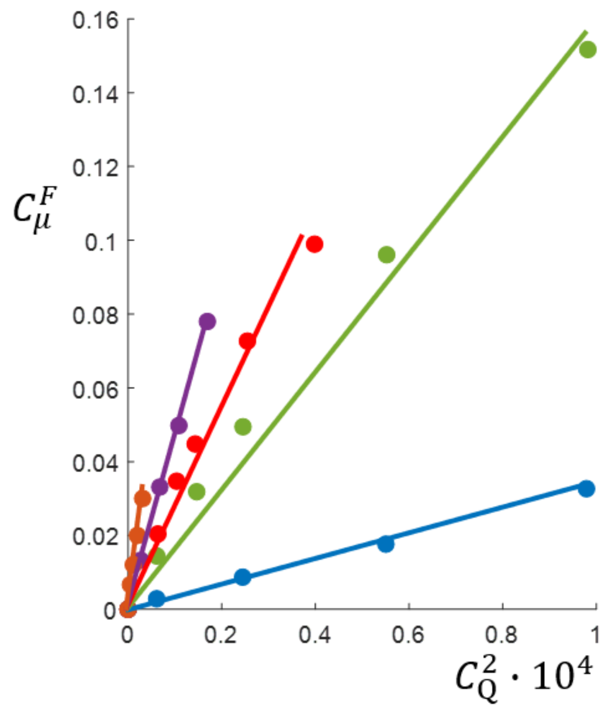

Figure 3. *Variation of C_μ^F with C_Q^2 for the 2-D actuation jet (●) and for the fluidically oscillating jet arrays with spanwise spacings of 0.16D (●), 0.33D (●), 0.49D (●), and 1.14D (●).*

To characterize the power requirements of the 2- and 3-D jets, the pressure and temperature of the air supply for actuation were measured inside the spar inlet outside the tunnel along with the actuation mass flowrate. Since the inlet temperature remained nearly ambient (19-21°C), the power (rate of heat and work) required from an ideal compressor to bring quiescent, ambient air to this inlet state is estimated from energy conservation to be $P_i = \frac{\dot{m}^3}{2}\left(\frac{RT_i}{p_i A_i}\right)^2$, where T_i and p_i are the temperature and pressure inside the inlet and A_i is the inlet cross-section. Based on this relationship, the inlet power coefficient $C_{\mathrm{IP}} = P_i/(\frac{1}{2}\rho {U_0}^3 DL)$ is calculated and compared with C_μ^F in Figure 4. For both the 2- and 3-D jets, the supplied C_{IP} varies nearly linearly with the effected C_μ^F. The inlet power required to achieve $C_\mu^F = 0.032$ for the densest array of 3-D jets is $C_{\mathrm{IP}} = 0.009$, while for the 2-D jet it is significantly higher $C_{\mathrm{IP}} = 0.217$ (not shown in Figure 4). For the 3-D jet spacings tested, the power required to effect a given C_μ^F decreases with sparser jet arrays. It should be noted that this disparity between the 2- and 3-D jets is predominantly driven by the disparity in required mass flow rate C_{Q} needed for the 2-D jets to effect the same level of C_μ^F the 3-D jet array, as seen in Figure 3.

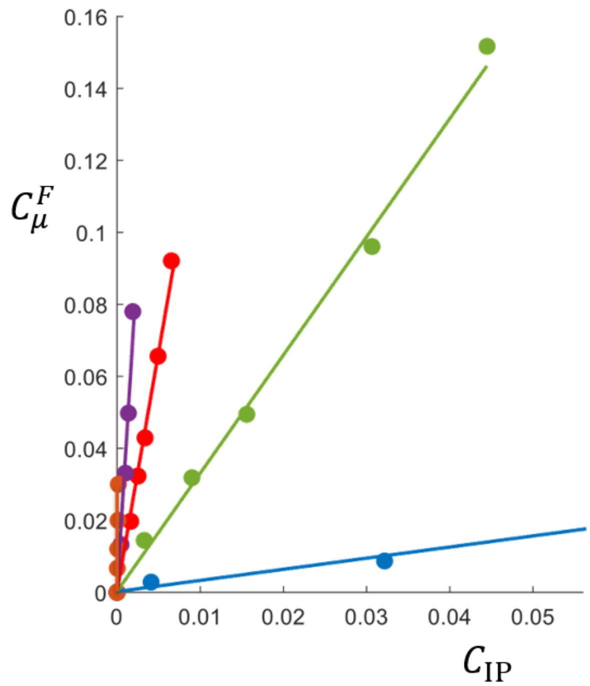

Figure 4. *Variation of C_μ^F with C_{IP} for the 2-D actuation jet (●) and for the oscillating jet arrays with spanwise spacings of 0.16D (●), 0.33D (●), 0.49D (●), and 1.14D (●).*

In addition to the surface static pressure measurements, the flow over the top surface of the cylinder and in its near wake was characterized by planar particle image velocimetry (PIV) in multiple spanwise-normal planes for several positions of the jet actuators. Each flow field was constructed from a set of eight partially overlapping views using a 2,640 × 2,300 pixel CCD camera, and the individual time-averaged flow fields were computed from ensemble averages of 500 instantaneous vector fields before being combined to form a single composite grid. The layout of PIV measurement planes is pictured in Figure 5a.

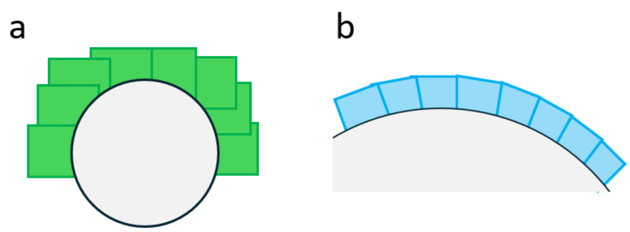

Figure 5. *Planar PIV views of the flow over top of cylinder and in the near wake (a, in green) and higher magnification views for boundary layer on the top surface of cylinder (b, in blue).*

To better resolve near-surface flow features, the boundary layer over the top of the cylinder was measured for several positions of the jet actuators using planar PIV in multiple spanwise-normal planes at a higher magnification of 6.8 μm/pixel for more spatial resolution. In these zoomed-in configurations, each PIV composite flow field was constructed from a set of eight partially overlapping views, where the time-averaged flow fields were computed from an ensemble averages of 500 instantaneous vector fields and overlayed on a single composite grid, as shown in Figure 5b.

III. THE AERODYNAMIC LOADS AND FLOW FIELDS OF 2- AND 3-D ACTUATION

The effects of the 2- and 3-D jets described in §II on the boundary layer and separating flow over the cylinder were characterized using planar PIV measurements in spanwise-normal *y*-*x* planes. As discussed by Higuchi et al. (1989), flow separation over smooth cylinders at critical Reynolds numbers is inherently spanwise nonuniform and is characterized by the appearance of cellular separation structures. Therefore, it was anticipated that the present base flow would also exhibit similar nonuniformities and that the flow structure in the cross-stream plane would vary along the span. For the purpose of characterizing the base flow in the presence of the inactive 2- and 3-D jets, the flow was mapped at the cylinder's center span ($z = 0$, Figure 6). The effects of the presence of the orifices of the actuation jets on the circumference of the cylinder were measured in the absence of actuation at two characteristic azimuthal position upstream and downstream ($\alpha = 80^o$ and 100^o) of the nominal location of separation over smooth cylinders at this subcritical Re_D. The data in Figures 6a and b show that the presence of the inactive 2-D jets results in a rather small difference in the flow fields; flow separates near $\theta \approx 90°$ and forms a detached shear layer of CW vorticity that extends into the wake while the reversed flow over the surface in the separated domain is marked by a thin layer of CCW vorticity along the surface. The presence of the inactive 3-D jets at $\alpha = 80°$ (Figure 6c) appears to be sufficient to trip the flow and delay the local separation to about $\theta \approx 100°$, as is evident by the downward turning of the separating shear layer (flow asymmetry between the top and bottom surfaces is manifested by variation of the lift and drag and is discussed in connection with Figure 7). However, when the 3-D jet array is moved to $\alpha = 100°$ (Figure 6d), the surface discontinuity at the jet orifices array does not affect separation

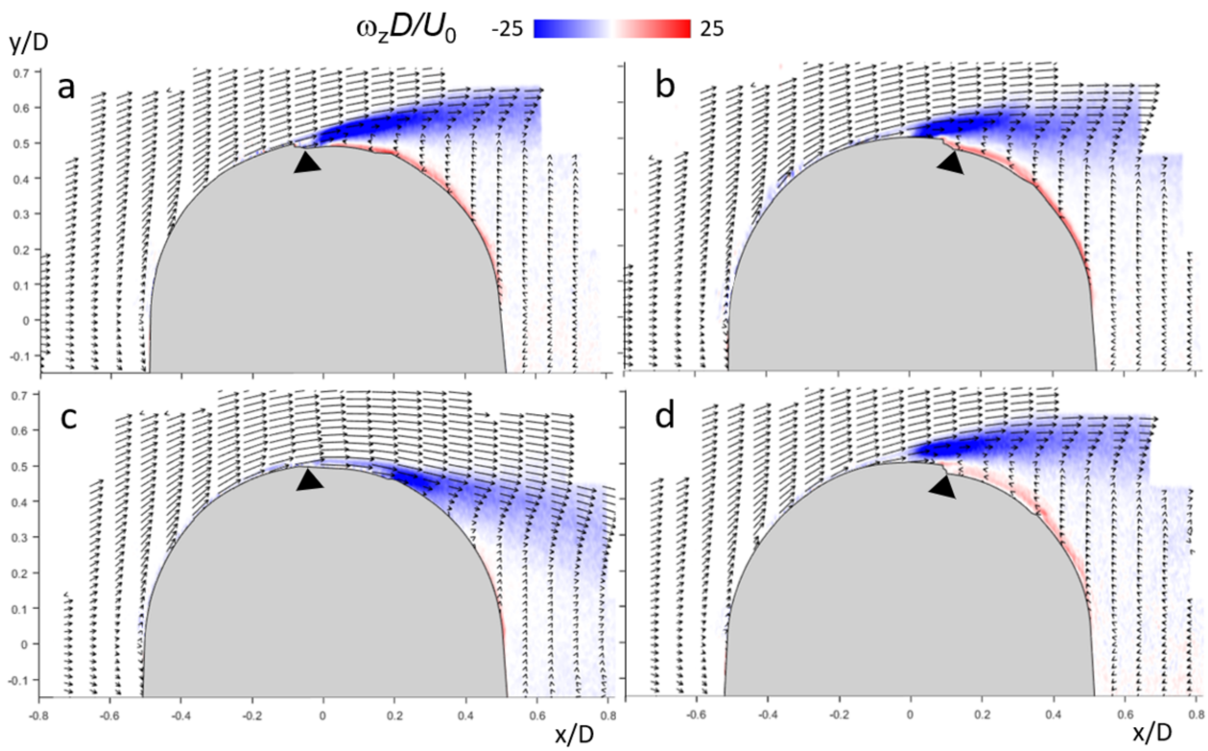

Figure 6. *Color raster plots of time-averaged spanwise vorticity concentrations overlaid with in plane velocity vectors in the base flow in the presence of the inactive 2-D (a, b) and 3-D (c, d) jets at α = 80° (a, c) and 100° (b, d).*

in the base flow and the measured flow field reverts to the flow in the presence of the inactive 2-D jets at the same azimuthal position in Figure 6b.

The main comparison between the aerodynamic loads induced by 3- and 2-D jet actuation (Figures 7 and 8, respectively) is conducted at 3-D jet spacings of 0.16D. As is shown by direct load cell measurements in Figure 7a, the lift in the base flow in the absence of actuation varies with the actuator position α, especially for $\alpha < 100°$, where the presence of the passive actuator orifices is on the windward side of the cylinder. It is noted that even with actuator orientations downstream of $\alpha = 100°$, the net lift does not vanish up to $\alpha = 140°$ ostensibly as a result of the spanwise variations in sectional lift owing to nonuniform separation. As expected, in the presence of actuation, the average lift induced by the 3-D jet array generally increases monotonically with the actuation level measured by C_μ^F. It is also noted that, for a given C_μ^F, the effected lift increases with α up to some critical position α_{crit}, beyond which lift declines precipitously. At the maximum present actuation level $C_\mu^F = 0.15$, the induced lift increases monotonically as with α reaching a maximum $C_L = 4.5$ at $\alpha_{crit} = 130°$. It is noted in passing that these measurements were acquired by setting α with the inactive jets and then activating the jets. Some limited measurements were also conducted by continuously increasing α in the presence of the active jets to verify that there were virtually no differences in the attained lift force or α_{crit}. Although not shown here, it is also noted that within this range of α time traces of the instantaneous lift were reasonably stable with standard deviations of about 0.1. For actuator positions $\alpha > \alpha_{crit}$, the time-averaged average lift begins to diminish and the instantaneous measurements of the aerodynamic loads exhibit larger amplitude fluctuations where at $C_\mu^F = 0.15$, the standard deviation of C_L increases to 0.4 at $\alpha = 135°$ and further to 0.8 at $\alpha = 140°$. These observations indicate increased flow unsteadiness past α_{crit} that is associated with interactions between the actuation jets and the spanwise nonuniform flow in the cylinder's boundary layer as further discussed in connection with Figure 11. These effects are also apparent in the nonmonotonic decrease in the lift past α_{crit} that are evident in Figure 7 indicating random bistable changes in lift that affect the time-averaged measurements. Similar trends in the lift are also apparent a $C_\mu^F < 0.15$, and when C_μ^F is sufficiently low, the actuation is susceptible to such unstable interactions with the surface boundary layer even below α_{crit}. The data in Figure 7 also show that the rates of change of C_L with α below and above α_{crit} are steeper at higher C_μ^F near α_{crit} but C_L sometimes deviates from this general trend as shown

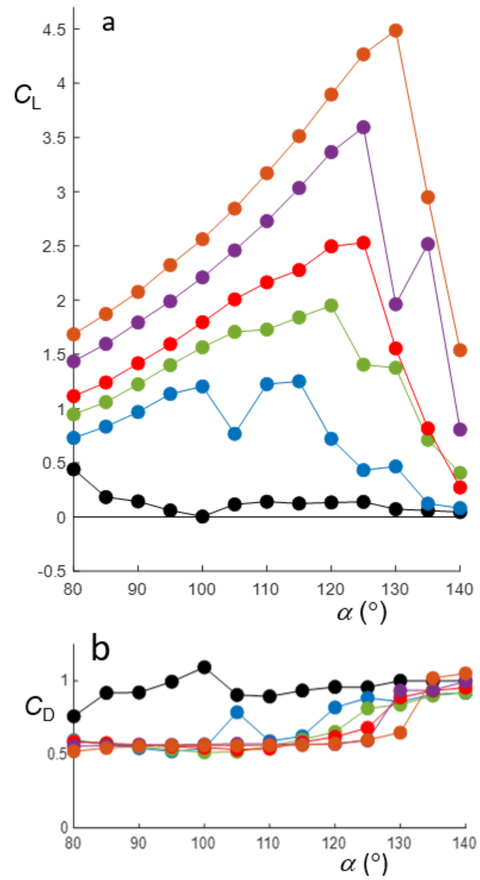

Figure 7. *Variation the normal load C_L (a) and streamwise load C_D (b) with the actuation position α for 3-D jets at $C_\mu^F = 0$ (●), 0.016 (●), 0.033 (●), 0.052 (●), 0.095 (●), and 0.151 (●).*

for example, at $\alpha = 105°$ for $C_\mu^F = 0.016$ and $\alpha = 130°$ for $C_\mu^F = 0.095$ (this can be attributed to long-range unsteadiness that is not equally captured by the limited measurement time series).

The corresponding drag data in Figure 7b show that the drag in the base flow also varies with α, especially for $\alpha < 100°$, which is attributed to the surface discontinuity at the jet orifices. However, even the lowest actuation level of $C_\mu^F = 0.016$ significantly reduces this variation, as the aerodynamic loads in the presence of actuation bypass the effects of the surface discontinuity. When the inactive jets are placed farther downstream $\alpha > 100°$, the baseline drag is $C_D = 0.95$, which is comparable to the drag on a smooth cylinder at $Re_D = 2 \cdot 10^5$ (Hoerner, 1965). Somewhat lower value of C_D than for the subcritical flow regime suggests an early stage of the drag crisis. When the actuators are placed downstream from α_{crit}, the drag reduction is diminished until about $\alpha \approx 130°$, where there is a small drag reduction at actuation levels $C_\mu^F < 0.095$ followed by a small drag increase at higher C_μ^F. The lift and drag data in Figures 7a and 7b indicate that the decrease in average lift near α_{crit} simultaneously weakens the net drag reduction.

The reduced sensitivity to variations with α of the lift and drag in the base flow that presumably are associated with general sensitivity to flow transition in the presence of jet actuation also indicates lower sensitivity to surface imperfections. As noted by Zdravkovich (1990), surface disturbances on a circular cylinder can lead to boundary layer transition and drag crisis at a lower Re_D and bypass the transitional flow regime. These effects are apparently realized at low actuation levels upstream of the apex that extend attachment and narrow the wake and lead to drag level of about 0.6 within the range of the natural drag crisis (e.g., Shih et al. 1993). The actuation jet can add a small contribution to the reduction when the jets are on the windward side of the cylinder.

The corresponding aerodynamic loads effected by the 2-D jets are shown in Figure 8. The range of 2-D actuation C_μ^F was lower due to limitations on the due to actuation mass flow rate that is required to achieve a given C_μ^F compared to the 3-D jets (cf. Figure 3). As shown in Figure 8a, the lift of the base flow in the presence of the inactive 2-D actuators ($h/D = 0.003$) varies less with α than in the corresponding base flow in the presence of the inactive 3-D jets ($h/D = 0.01$). As with the 3-D jets, the lift induced by the 2-D jets increases monotonically with C_μ^F for $80° < \alpha < 130°$. At the higher actuation levels ($C_\mu^F = 0.0087, 0.018, 0.032$) there is a monotonic increase in lift with α from $\alpha = 80°$ to $\alpha_{crit} = 100°$, followed by a decrease from $\alpha = 100°$ to 130°. The maximum lift generated by the 2-D jets in the present measurements is $C_L = 1.4$ for $C_\mu^F = 0.033$ at $\alpha_{crit} = 100°$, which is comparable to the lift generated in the investigations of Ghee and Leishman (1992) who used a 2-D jet at $\alpha = 90°$ blowing and $C_\mu^F = 0.04$. The lower actuation level $C_\mu^F = 0.003$ produces very little lift except at $\alpha = 95°$, where $C_L = 0.24$. Time series of the lift (not shown)

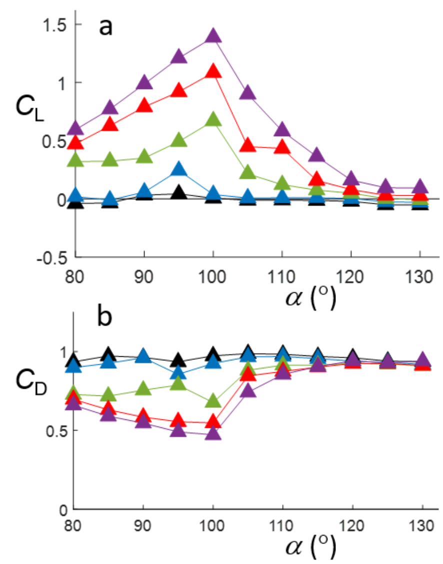

Figure 8. *Variation the normal load C_L (a) and streamwise load C_D (b) with the actuation position α for 2-D jet at $C_\mu^F = 0$ (▲), 0.0028 (▲), 0.0087 (▲), 0.018 (▲), and 0.032 (▲).*

effected by the 2-D jet at higher actuation levels (C_μ^F = 0.018, 0.032) are relatively steady for $\alpha < \alpha_{crit}$, with standard deviation of about 0.08, that increases to 0.15 at $\alpha > \alpha_{crit}$, similar to what was observed for the 3-D jets owing to increased non-uniformity of lift in the span that is discussed in connection with Figure 11. Similar to the 3-D jets, the rates of change of C_L with α below and above α_{crit} are steeper at higher levels of C_μ^F.

Figure 8b shows that the drag coefficient of the base flow with the inactive 2-D jets is about 0.95 and nearly invariant with α. Drag reduction with actuation is most prevalent for $\alpha \le \alpha_{crit}$, with the largest reduction of 53% at C_μ^F = 0.033 at α_{crit} = 100° which is comparable to the drag reported by Ghee and Leishman (1992, $Re_D = 1.9 \cdot 10^5$) with C_μ^F = 0.07 at α = 100° and trips at θ = 60° and 300°. Higher actuation levels (C_μ^F = 0.018, 0.032) lead to the largest monotonic decrease in drag with α while lower actuation levels (C_μ^F = 0.009, 0.018) yield lower reduction (C_μ^F = 0.0087 only significantly reduces the drag at α = 95°). The monotonic decrease in drag with α here is also attained with the 3-D jets for 80° < α < 100° for the similar C_μ^F (0.016 and 0.033, cf. Figure 7b). For actuator positions further downstream than α_{crit}, drag reduction diminishes with α until it asymptotically approaches the base flow level at α = 120°.

As shown in Figure 3, at the same actuation mass flow rate coefficient of C_Q = 0.010, the attained momentum coefficients of the 2- and 3-D jets are C_μ^F = 0.032 and 0.15, respectively. At these conditions, the 2-D jets yielded maximum lift of C_L = 1.3 at α = 100° while the 3-D jets yielded a maximum lift that is about 3.4-fold higher of C_L = 4.5 at α = 130° (cf. Figure 3). The lift effected by the 2- and 3-D jets is more comparable at a common actuation momentum coefficient, and the remainder of this section focuses on the performances of the 2- and 3-D actuators at $C_\mu^F \approx$ 0.032 and 0.033. Figure 9a indicates a consistently better performance of the 3-D jets as the actuation angle α increases from α = 80° up to α = 100° (α_{crit} for the 2-D jet configuration) after which the difference relative to the 3-D jets broadens until their α = 120° (α_{crit} for the 3-D jet configuration), where the 3-D jets generate C_L = 2 and the lift induced by the 2-D jets nearly vanishes. As discussed in connection with Figure 13, the jet-induced lift is associated with the suppression of separation and turning of the outer flow on the actuated side of the cylinder. It is conjectured that the disparity in α_{crit} between the 2- and 3-D jets is related to the differences between the spanwise distributions of their momentum coefficients. Namely, the 2-D jets effect lower nearly-uniform momentum while the 3-D jets effect higher, highly localized momentum. While the uniformly-distributed C_μ^F of the 2-D jets apparently fails to affect flow separation at higher α, the localized high levels of C_μ^F of the 3-D jets effect spanwise-discretized flow attachment across the span at α past α_{crit} of the 2-D jets. Past the critical angle of the 3-D

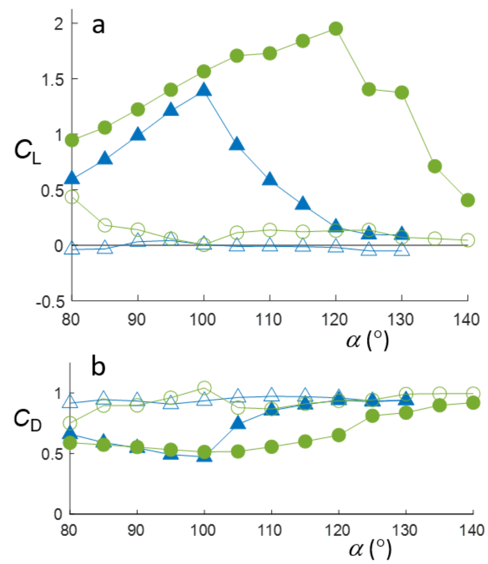

***Figure 9**. Variation of C_L (a) and C_D (b) with α at $C_\mu^F \approx 0.032$ for the 2-D jet (▲) and the 3-D jet (●). The corresponding variations in the base flow in the presence of the inactive actuators are shown using (Δ) and (○).*

jets the induced lift decreases gradually (on average), compared to the vanishing effect of the 2-D jets at these angles. It is noted that even at the maximum lift generated by the 2-D jet (C_L = 1.4 at α = 100°), the 3-D jets still induce somewhat higher lift, although the difference between the 2-D and 3-D jets is lowest at that angle. Although the lift generated by both actuator types increases monotonically with α upstream of their respective α_{crit}, the rate of increase for the 2-D jet is ~30% higher. The decline of lift generation past α_{crit} occurs at a similar rate with α for both the 2- and 3-D jets. As shown in Figure 9b, both the 2- and 3-D jets provide drag reductions of about 40% upstream of their respective α_{crit}. For 80° < α < 100°, the actuated drag decreases monotonically with α for both actuator configurations, where the rate of decrease is about 2.5 times larger for the 2-D jet. Similarly to the lift effect, the drag reduction for the 3-D jets persists past the α_{crit}, of the 2-D jets albeit with some relaxation for α > 100°.

The time-averaged azimuthal static surface pressure distributions over the cylinder $C_P(\theta)$ in the presence ($C_\mu^F \approx 0.032$) and absence ($C_\mu^F \approx 0$) of actuation by the 2- and 3-D jets were measured at the spanwise position z = 1.77D (z = 0 is center span) and are shown in Figure 10 for α = 100° and 115°. In the base flow pressure distributions (in presence of the inactive actuators), the pressure distributions over the top and bottom surfaces are nearly symmetric with small suction peaks of C_P = -1.3 at θ = +/- 70° with nearly no variations in the base pressure $C_P \approx$ -1.0 for 95° ≤ α ≤ 275° within the separated flow. In the presence of actuation at α = 100°, the 2-D jets effect C_L = 1.4, which is reflected in the asymmetric pressure distribution in Figure 10a. This distribution has an suction peak C_P = -3.2 at θ = 72°, a diminished suction peak C_P = -0.91 at θ = 285°, and a smaller separated domain 155° < θ < 255° with a higher base pressure C_P = -0.65. By comparison, the 3-D jets at α = 100° yield C_L = 1.6 corresponding to an accentuated asymmetry of the pressure

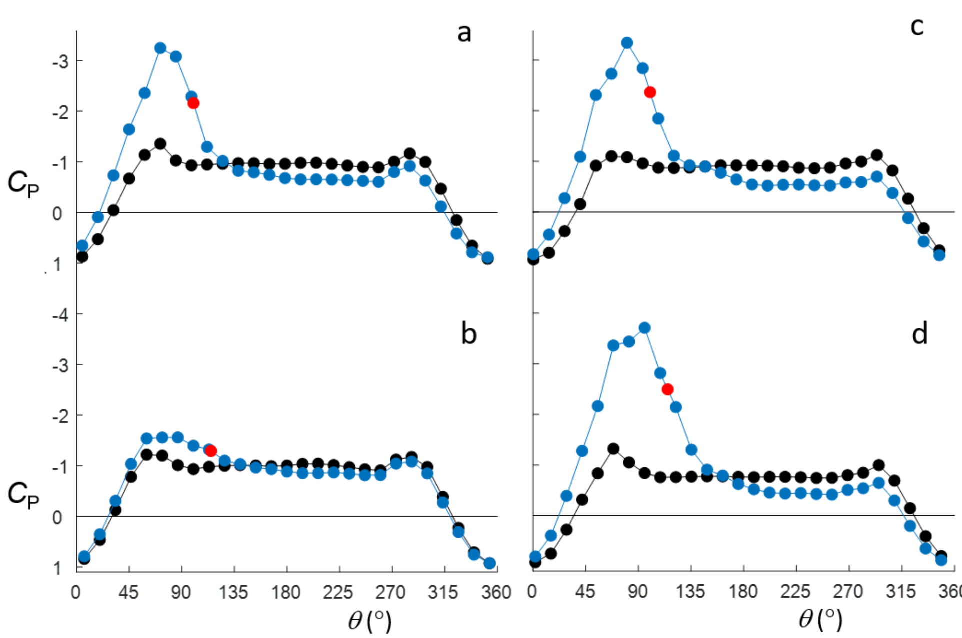

Figure 10. *Variation of C_P with θ in the presence of the 2-D jets (a, b, c) and 3-D jets (d, e, f) for C_μ^F = 0 (baseline, ●) and 0.032 (●) measured at z = 1.77D for α = 100° (a, d), 115° (b, e), and 130° (c, f). Actuator positions α are indicated in red (●).*

distribution in Figure 10c with a suction peak C_P = -3.3 at θ = 80°, a diminished suction peak C_P = -0.70 at θ = 294°, and a smaller separated domain 186° < θ < 280° with higher base pressure C_P = -0.54. The suction peak effected by the 3-D jets also has a domain 120° < θ < 186° with C_P = -0.90 that is lower than the base pressure, that can be attributed to a direct local Coanda effect of the jets. The 2-D jet at α = 115° is far downstream of α_{crit} = 100° and the resulting lift coefficient is only C_L = 0.36, which is reflected in the slightly asymmetrical actuated pressure distribution in Figure 10b that has a slightly augmented suction peak C_P = -1.6 at θ = 75°, an opposite suction peak that is mostly unchanged at θ = 290°, and a smaller separated region 170° < θ < 260° with a slightly higher base pressure C_P = -0.85. Since the 3-D jets at α = 115° are still upstream of their α_{crit} = 120°, they induce considerably higher lift C_L = 1.8, which is reflected in the asymmetric pressure distribution in Figure 10d that is similar to the distribution in Figure 10c at α = 100°, but with higher suction peak C_P = -3.7 that extends farther downstream such that the separated domain is within 200° < θ < 270° and the base pressure increases to C_P = -0.43. Its opposing suction peak also shrinks to C_P = -0.65.

Figure 11 compares the variation with C_μ^F of the lift effected by each of the 2- and 3-D actuation jets as measured by the load cells to the lift inferred from integrated pressure distribution measured at z = 1.77D. While the lift measured by the load cells accounts for inherent variations in separation along the span (e.g., Higuchi et al., 1989) the lift inferred from the local measurement is affected by the specific state of the flow at this spanwise position. Figures 11a-d compare the local/global lift for the 2-D jets α = 100°, 105°, 110°, and 115°, respectively for C_μ^F < 0.032. Figures 11e-h compare the local/global lift for the 3-D jets α = 120°, 125°, 130°, and 135°, respectively for C_μ^F < 0.15. For both the 2-D and 3-D jets, the global and local lift generally agree for $\alpha \le \alpha_{crit}$, as is shown in Figures 11a and e. With the 2-D jet at α = 100° and C_μ^F = 0.032 (Figure

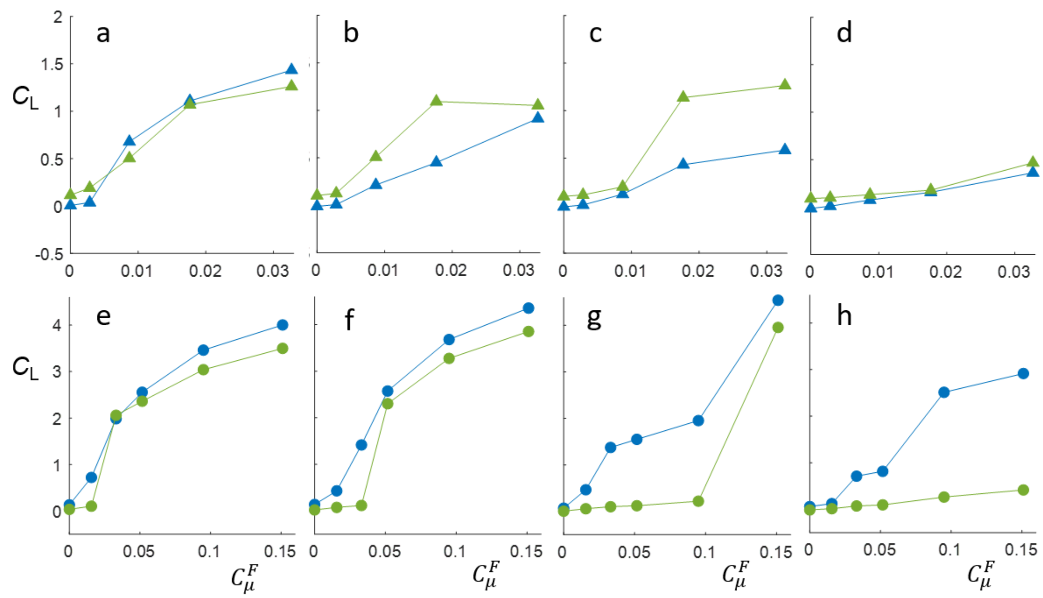

Figure 11. *Variation of C_L with C_μ^F for the global C_L measured on the load cells (▲, ●) and local C_L inferred from local azimuthal pressure distribution at z = 1.77D (▲, ●): 2-D jet at α = 100°, 105°, 110°, and 115° (a, b, c, d) and 3-D jets at α = 120°, 125°, 130°, and 135° (e, f, g, h).*

11a), the local pressure lift is 10% lower than the global lift while with the 3-D jets at $\alpha = 100°$ and $C_\mu^F = 0.032$ (Figure 11e) the local pressure lift is 12% lower than the global lift. These differences may be attributed in part to spanwise gaps between the actuators (cf. §II). As the 2-D jet is shifted to $\alpha = 115°$ in Figures 11b, c, and d, both the local and global lift diminish to $C_\mathrm{L} \approx 0.4$ at $C_\mu^F = 0.032$ and $\alpha = 115°$. However, the monotonic decrease of the global lift with α outpaces the decrease of the local lift, which decreases slightly for at the higher actuation levels ($C_\mu^F = 0.018$, 0.032) before dropping sharply from $\alpha = 110°$ to 115°. The differences between the local and global lift indicate that, at least for some actuator positions $\alpha > \alpha_\mathrm{crit}$, the flow induced by the 2-D jet is sufficiently 3-D to produce spanwise regions with different circulation and that the single azimuthal pressure distribution is not sufficient for estimating the total lift. The pattern of higher local lift compared to the global lift generated by the 2-D jet at $\alpha = 105°$ and 110° indicates that the pressure measurements at $z = 1.77D$ fall within a cell of suppressed separation during actuation in a flow with spanwise-varying attachment. The presence of such cells is not unexpected at subcritical Re_D as noted by and Higuchi et al. (1989).

As the 3-D jets are shifted from $\alpha = 120°$ to 125° in Figure 11f, the local lift at $C_\mu^F = 0.012$ falls sharply with α from $C_\mathrm{L} = 2.1$ to 0.03. Higher actuation levels lead to similar sharp decreases in lift at $\alpha > \alpha_\mathrm{crit}$ with $C_\mu^F = 5.2\%$ and 9.5% dropping at $\alpha = 130°$ in Figure 11g and $C_\mu^F = 15\%$ dropping at $\alpha = 135°$ in Figure 11h. In contrast, the global lift does not undergo similar sharp drops with α but gradually decreases after α_crit for each C_μ^F. In common with the 2-D actuation the difference between the local and global lift shows that the 3-D flow induced by the 3-D jets produces spanwise domains with different circulations. The pattern of lower local lift compared to the global lift generated by the 3-D jets for $\alpha = 125°$ to 135° suggests that, for $\alpha > \alpha_\mathrm{crit}$, the pressure measurements at $z = 1.77D$ fall outside of some remaining cells in which separation is suppressed by the actuation. The presence of such cells was observed by Rackers et al. (2024) on the suction surface of the cylinder and in its near wake.

Figure 12 shows color raster plots of the in-plane turbulent kinetic energy (TKE) for the base flow in the presence of the inactive 2- and 3-D actuators and in the presence of actuation by the 2- and 3-D jets at $C_\mu^F \approx 0.032$ and at $\alpha = 80°$, 100°, and 120°. These data show that the highest levels of TKE are measured near separation and in the ensuing shear layer. The base flow in Figure 12a separates at $\theta \sim 90°$, with a concentration of TKE in the shear layer and partially at the end of the measurement domain, close to the wake core. Figure 12b shows that with 2-D actuation at $\alpha = 80°$, separation is shifted downstream to $\theta \sim 112°$. Additionally, the shear layer core has slightly enhanced TKE relative to the base flow and is deflected by 8° towards the model centerline. As the 2-D jet actuation is shifted downstream to $\alpha_\mathrm{crit} = 100°$ (Figure 12c), the flow attachment is extended to $\theta \sim 135°$ and the shear layer is also further deflected by 17° towards the model centerline with a significantly diminished TKE core. The further deflection of the outer flow and associated increase in flow asymmetry corresponds to an increase in lift from $C_\mathrm{L} = 0.59$ at $\alpha = 80°$ to $C_\mathrm{L} = 1.4$ at $\alpha = 100°$. As the 2-D jets are moved to $\alpha = 100°$it overcomes the wake in the base flow and extends attachment. Figure 12e shows that with the actuated 3-D jets at $\alpha = 80°$, separation is shifted downstream to $\theta \sim 145$, while the shear layer is deflected by 23° towards the model centerline. With the 3-D jets at $\alpha = 100°$ (Figure 12f), separation is suppressed further to $\theta \sim 166°$, while the thinner shear layer is also vectored by 31° towards the model centerline. Similar to the 2-D jet, this further deflection of the outer flow corresponds to an increase in lift

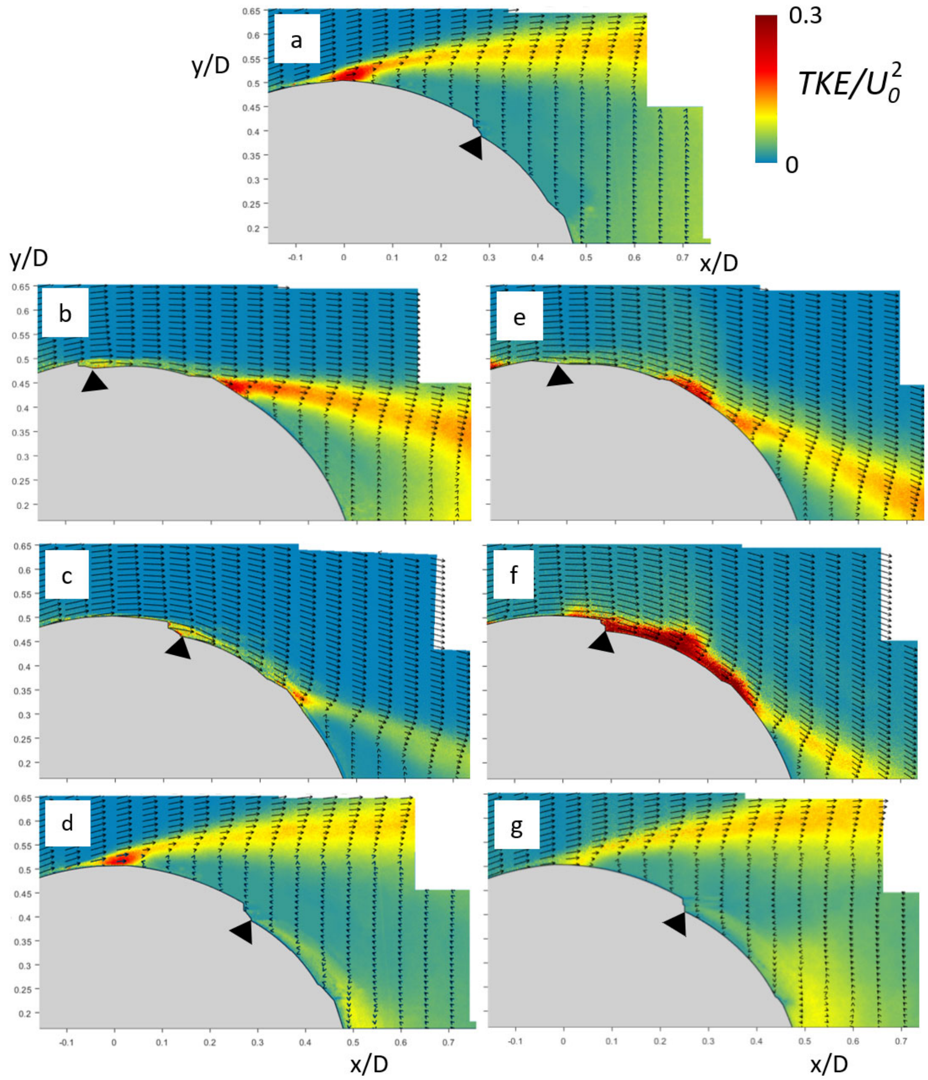

Figure 12. Normalized TKE contours at center span around baseline cylinder with actuators in wake (a), around the actuated cylinder with the 2-D jet at C_μ^F = 0.032 and α = 80°, 100°, and 120° (b, c, d), and around the actuated cylinder with 3-D jets at the same C_μ^F and α values (e, f, g).

from C_L = 0.90 at α = 80° to C_L = 1.6 at α = 100°. There is additionally a concentration of TKE effected by the 3-D jets at θ = 100° that persists through separation at $\theta \approx$ 166° that marks the associated entrainment of the wake by the fluidically oscillating jets over the cylinder surface. At the common $C_\mu^F \approx 0.032$ at α = 80° and 100°, the 3-D jet array suppresses separation azimuthally by about 33° further downstream than the 2-D jet and deflects the shear layer by about 15° further towards the model's centerline, in agreement with the higher lift effected by these jets (cf. Figure 9a). Finally, when the actuation arrays are placed at α = 120° (Figures 12d, g), separation in this plane is not suppressed and remains at $\theta \sim$ 90°, with the undeflected shear layer remaining. The jets issuing from the 2- and 3-D actuators do not have enough authority to attach the separating flow at $\theta >$ 120° at $z = 0D$ as noted by the presence of the jets issuing along the base surface of the cylinder in the separated wake. However, the 3-D jets still yield a significant lift C_L = 0.75, suggesting the presence of attachment cells outside of the PIV-measured plane. While the issued

2-D jet remains close to the surface, the 3-D jets couples to the wake, as is shown in the higher TKE levels away from the surface. The 3-D jets promote more entrainment and mixing compared to 2-D jet, especially in the turbulent interactions between adjacent jets (Rackers et al., 2024).

IV. THE EFFECTS OF TRIPPED BOUNDARY LAYER ON THE INDUCED AERDODYNAMIC LOADS

As noted in §III, the present experiments are conducted at a subcritical Reynolds number ($Re_D = 2.1 \cdot 10^5$) near the critical value over a nominally smooth circular cylinder where the surface boundary layer is nominally transitional (e.g., Achenbach and Heinecke, 1981). In order to assess the effects of boundary layer transition to turbulence on the aerodynamic loads effected by the 3-D jets, the flow over the cylinder was forced using a conventional trip that at critical Reynolds numbers leads to a significant diminution in drag within the ‘drag crisis’ between the subcritical and supercritical Reynolds numbers. In this flow regime, the boundary layer over the cylinder is sensitive to surface roughness, free stream turbulence levels, and boundary conditions.

An important aspect of this flow regime was discussed by Higuchi et al. (1989) who pointed out a cellular separation structure across the span of a cylinder at subcritical Reynolds numbers akin to stall cell patterns on airfoils (Schewe, 2001) which leads to significant spanwise nonuniformity of separation over the 2-D cylinder. These later stages of the transition can also be associated with temporal variations of the flow due to momentary reattachment and separation. These complexities at critical Reynolds numbers have been traditionally bypassed by intentional boundary layer tripping upstream of the cylinder apex to enforce transition in a somewhat controllable manner. Early studies pointed to added complexities associated with the trip size and its azimuthal placement. Igarashi (1986) noted different scenarios in which the tripped flow remains laminar with little or no effect, transitions to turbulence inducing extended attachment, or directly couples to the adverse pressure gradient and remains separated. Further experimental assessment of the significance of the position of the trip wire were conducted by Ekmekci and Rockwell (2010), who identified two critical azimuthal positions either resulting in flow reattachment downstream from the trip followed by bistable separation that suppresses the Karman instability, or (at higher angle) where the tripped flow becomes directly coupled to the wake, which amplifies Karman instability. Following the experimental findings of Igarashi (1986), a numerical investigation by Chopra and Mittal (2022) classified transitions due to a trip as ‘natural’, when the trip induces a laminar separation bubble, and ‘direct’, when the trip disturbs the BL enough to induce turbulent reattachment past the trip. Moreover, these authors showed how disturbances induced by a small trip are advected but subsequently grow in the adverse pressure gradient and can lead to extended attachment. When the trip is sufficiently tall, the vortices are shed directly from the trip, and when generated close to the apex they can directly couple to the separating shear layer without reattachment.

In order to promote transition in a controllable manner, the present investigations utilized a small trip of thickness $t/D = 0.0013$ that was placed across the full span of the cylinder surface. First, in the absence of actuation, the trip effect was tested at azimuthal orientations $\theta = 30°$, 45°, 60°, 75°, and 90°, with maximum lift realized at $\theta = 60°$ ($C_L = 0.68$), comparable to what was achieved with 2-D jet actuation for $\alpha = 90°$ and $C_\mu^F = 0.018$, or for $\alpha = 85°$ and $C_\mu^F = 0.032$ (cf. Figure 8a). This level of lift is comparable to the passive lift of $C_L = 0.75$ generated in a similar experiment by

Chopra and Mittal (2022) with a trip of height $t/D = 0.01$ at $\theta = 78°$, $Re_D = 2\cdot10^5$. The large increase in lift associated with the presence of the trip highlights the sensitivity of the baseline aerodynamic loads to small surface perturbations in transitional flow regime. Initial tests of the controlled flow in the presence of tripping involved the same trip azimuthal orientations, having the active 3-D jets positioned at $\alpha = 115°$ with actuation levels C_μ^F = 0.016, 0.033, 0.052, 0.095, and 0.151. It was found (not shown) that the addition of the trip did not significantly alter the lifts produced in the absence of a trip (Figure 7a).

However, an interesting phenomenon was observed when keeping the trip position fixed at $\theta =$ 60° and varying the jets' location at $\alpha = 110°$, 115°, 120°, 125°, and 130°. Figure 13 illustrates the resulting variation of C_L with C_μ^F for each of the 3-D jets' angles, for both the smooth and tripped cylinder flow. Lift varies minimally with α in the absence of actuation, with $C_L \sim 0.07$ for the untripped cylinder and $C_L \sim 0.6$ using the trip. With actuation at $\alpha = 110°$ (Figure 13a), in the absence of the trip, lift increases to $C_L = 3.1$ for $C_\mu^F = 0.15$, and in the presence of the trip, a small additional lift increment ($\Delta C_L = 0.2$) is present for $C_\mu^F = 0.15$, but, in principle, both evolutions are notably close. A similar trend is seen for $\alpha = 115°$ (Figure 13b), where the tripped flow, in spite of a higher zero bias, relatively closely follows the lift evolution of the untripped flow. Hence, the trip has minimal effect on C_L at both of these angles. As the actuators are moved farther downstream, tripping leads to a gradual loss of the attained lift of the untripped flow. At the next angle $\alpha = 120°$ (Figure 13c), some loss of lift is noted with the addition of the trip for intermediate C_μ^F, but the untripped lift levels are still maintaned for the highest C_μ^Fs. However, the noted drop in C_L becomes exacerbated at the next angle of $\alpha = 125°$ (Figure 13d), where the jets acting on the tripped flow effect substantially lower C_L than those acting on the untripped flow for $C_\mu^F > 0.02$. The tripped flow becomes even less sensitive to increasing C_μ^F at the highest angle $\alpha = 130°$ (Figure 13e), maintaining the similar trend seen in Figure 13d, and the presence of the trip leads to significantly reduced lift increment, with a maximum lift of $C_L = 1.5$ at $C_\mu^F = 0.15$. The reduced effectiveness of the actuation due to tripping is especially prominent for $\alpha = 125°$ and $C_\mu^F = 0.095$, as well as for $\alpha = 130°$ and $C_\mu^F = 0.15$, with reductions in lift increment of $\Delta C_L = 1.8$ and 3.0, respectively. For a given C_μ^F, loss of lift is most pronounced at actuator positions near α_{crit} for the untripped cylinder. In a similar experiment involving lift generation by a 2-D jet, Ghee and

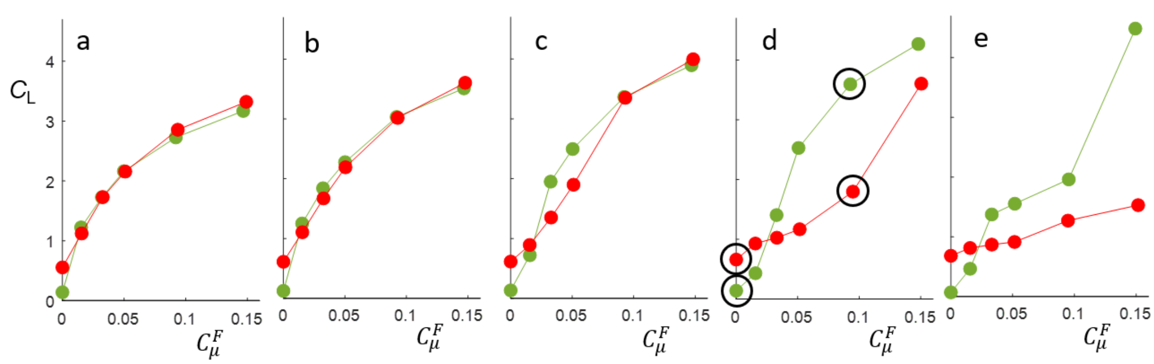

Figure 13. *Variation of C_L with C_μ^F from 3-D jets, with actuator positions α = 110° (a), 115° (b), 120° (c), 125° (d), and 130° (e), without tripping (●) and with a trip at θ = 60° (●). Four significant cases referenced in Figures 14-20 are circled.*

Leishman show a lift reduction of $\Delta C_L \sim -1$ with the addition of trips at $\theta = 60°$ and 300° for $\alpha = 90°$ and $C_\mu^F = 0.07$ (1992, $Re_D = 1.9 \cdot 10^5$).

The distinctive lift decrement from placing the trip at $\theta = 60°$ while actuating at $\alpha = 125°$ and $C_\mu^F = 0.095$ (circled in black in Figure 13d) is explored further by the probability density functions of the instantaneous C_L in Figure 14. Figure 14a shows that the lift fluctuations on the untripped cylinder at baseline are nearly symmetric around $C_L = 0$ with a standard deviation of 0.26 and a small asymmetric tail extending to $C_L \sim 1$, which contributes to the small non-zero baseline lift from asymmetric boundary layer transition over both sides of a cylinder, which was also noted in smooth cylinder experiments in transitional flow ($Re_D = 1 \cdot 10^5$ to $3 \cdot 10^5$) by Szepessy and Bearman (2006). Adding the $\theta = 60°$ trip to the baseline geometry skews the average lift coefficient to $C_L = 0.54$ with a tighter standard deviation of 0.09 (Figure 14b). The smaller lift fluctuations may correspond to the reduced shear layer/wake unsteadiness under the tripped conditions. In the case of the untripped cylinder flow actuated by $C_\mu^F = 0.095$ (Figure 14c), there is a high average lift of $C_L = 3.4$, an indication of the flow's prolonged attachment with actuation. It is interesting that the probability density function of this actuated flow is nearly a mirror of the baseline distribution (Figure 14a), but with a longer tail extending into the lower lift values from $C_L \sim 1$ to 3 and a higher standard deviation of 0.47. The skew in the direction of the baseline lift can be attributed to occasional re-separation of the predominantly attached flow, likely in a non-uniform fashion across the span. When the tripped flow is controlled by the same actuation level $C_\mu^F = 0.095$ (Figure 14d), there is a wide variation of lift about a lower average level of $C_L = 1.5$. The high standard deviation of 0.56 and the tails of the distribution extending from $C_L = 0$ to 4 indicate an oscillation between almost no suppression of separation (the jets issuing into the separated wake) and significant

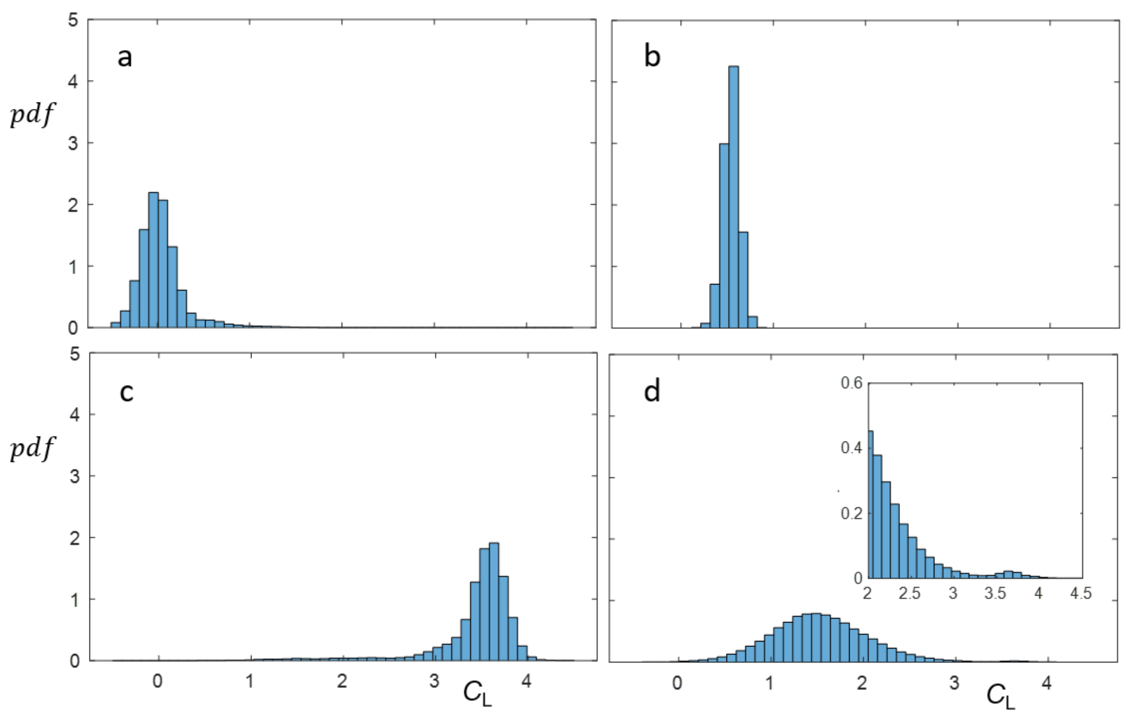

Figure 14. *Probability density function of C_L for $C_\mu^F = 0$ (a, b) and 0.095 (c, d) without tripping (a, c) and with $\theta = 60°$ trip (b, d).*

suppression of separation across the cylinder span, with various spanwise nonuniformities that produce the fully populated realizations of lift between the extremes. A small peak in the probability density function exists for this case at $C_L = 3.7$ (emphasized in the inset plot), which is close to the primary probability density peak of the untripped actuated flow in Figure 14c, indicating an unstable occasional reversion to a fully attached flow field in the presence of the trip.

After assessing the unsteady nature of lift generation both in natural and controlled flows, Figure 15 shows the dominant frequencies associated with the time-traces of lift for the untripped (Figure 15a) and tripped (Figure 15b) flows discussed in Figure 14. The baseline untripped flow shows a multi-peak distribution at about 300 Hz, where the most prominent peaks correspond to Strouhal numbers $St = 0.18$ and 0.2, where the latter is a classical Strouhal number typically associated with cylinder flows. Also, the peak of $St = 0.18$ was previously reported for a smooth circular cylinder flow by Bearman (1969) for the same Reynolds number range of $Re_D = 2 \cdot 10^5$. Once the untripped flow is actuated, this multi-peak broadens, becoming void of individual peaks while also shifting towards the central $St = 0.15$. Simultaneously, energy across most scales becomes elevated, especially across the lower spectrum. The intensification of low-frequency lift oscillations may correspond with the larger amplitude variations in lift while the jets at α_{crit} keep the outer flow marginally attached. The tripped baseline lift in Figure 15b exhibits features of the smooth cylinder flow both with and without control: there are two prominent peaks within a broad spectral peak, but the main peak is centered about $St = 0.15$, just like in the case of the controlled untripped flow. Once the tripped flow is controlled, a strong shift across all the frequencies is seen (Figure 15b), having a broad, but narrower than in the case of untripped flow, peak at somewhat lower $St = 0.14$.

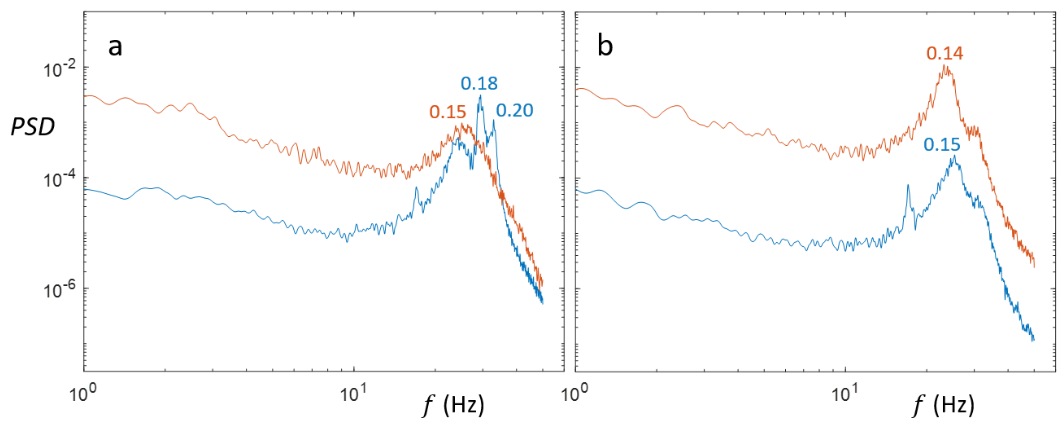

Figure 15. *Power Spectral Density of C_L versus frequency without tripping (a) and with $\theta = 60°$ trip (b) for C_μ^F = 0 (blue) and 0.095 (orange). Spectral peaks are labelled with corresponding Strouhal numbers.*

To further investigate the reduced lift increment from actuation in the presence of tripping, sets of 8 partially overlapping high-magnification planar PIV views were captured at $z/D = -1.18$ to resolve the boundary layer for $60° \leq \theta \leq 145°$ for the same four cases circled in Figure 13. Figure 16 shows the resulting in-plane time-averaged velocity vectors and velocity magnitude contours above the cylinder surface for $82° \leq \theta \leq 145°$. For the untripped cylinder without actuation (Figure 16a), the flow separates at $\theta \sim 80°$, compared to $\theta \sim 90°$ at the centerline ($z/D = 0$) plane (cf. Figure 6), which together with a PIV survey of several other spanwise planes (not shown) further supports an earlier assessment about spatial nonuniformities in the transitional flow over a cylinder, a phenomenon also noted for transitional flow on a circular cylinder by Higuchi, Kim, and Farell

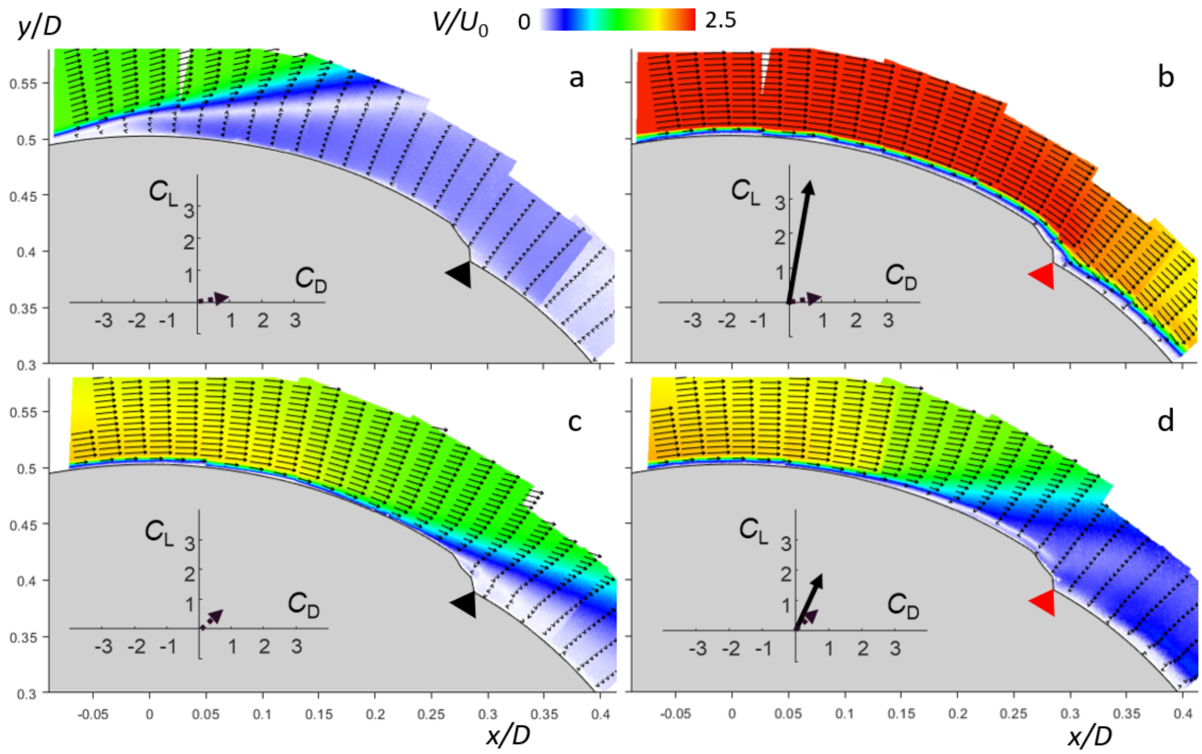

Figure 16. *Time-averaged flow fields in spanwise-normal plane and color contours of in-plane velocity magnitude over cylinder with 3-D actuators at α = 125° for untripped cylinder (a, b) and tripped cylinder (θ = 60°; c, d), as well as C_μ^F = 0 (a, c) and 0.095 (b, d). The magnitude and direction of total aerodynamic load is shown within each cylinder profile, with dashed arrows for C_μ^F = 0 and solid arrows for C_μ^F = 0.095.*

(1989). A closer look at the composite flow field reveals small mismatches between individual flow fields of the composite, which is also attributed to small variations of separation location between individual flow measurements across multiple windows, a possible indication of a long-range temporal variations of separation. The maximum time-averaged speed above the cylinder is V/U_0 = 1.6, and the resulting aerodynamic force (denoted as lift and drag in inset plot) indicates a small passive lift of C_L = 0.13 and a drag of C_D = 1.0. Once this baseline flow is controlled by C_μ^F = 0.095 (Figure 16b), the flow remains attached downstream of θ = 145°, having an accelerated outer flow (maximum speed over the cylinder of V/U_0 = 2.7) and a clear indication of a thin boundary layer through the adverse pressure gradient, resulting in the lift increase to C_L = 3.6 and drag reduction to C_D = 0.6. The actuator location (α = 125°) is at α_{crit} for C_μ^F = 0.095 and therefore moving the actuators downstream at this actuation level would reduce the lift increment (cf. Figures 13d, e).

The baseline tripped flow (trip at θ = 60°, Figure 16c) exhibits enhanced attachment on the tripped surface side compared to the absence of tripping (or over the opposite side), with the flow separating immediately upstream of the jet array at $\theta \sim$ 116°, and there is correspondingly a passive lift of C_L = 0.66. With tripping, the maximum speed over the baseline cylinder is increased to V/U_0 = 2.0, and the drag is reduced to C_D = 0.6, as in the presence of actuation without the trip. After the control jets are activated at C_μ^F = 0.095 (Figure 16d), the effected lift of C_L = 1.8 is lower than that of the untripped cylinder flow with actuation (C_L = 3.6). The time-averaged velocity field represents the average of multiple instantaneous realizations, with separation occurring in some realizations near $\theta = 110°$ and in others at $\theta > 145°$, as is reflected in the relatively high standard deviation of C_L, with a value of ~0.4. The slight mismatches of average in-plane flow fields in the composite view reflect variation in the fraction of time that the flow undergoes time-varying separation, which was already shown to energize low-frequency (long range) states under the controlled flow conditions. The aerodynamic loads induced by actuation on the tripped cylinder vary both spatially and temporally, which is similar to the loads for actuator positions downstream of α_{crit} (cf. Figure 11).

Clearly, the most interesting realization of the controlled cases discussed in Figures 14 – 16 is the somewhat unexpected loss of effectiveness of the control jets fixed at $\alpha = 125°$ for the tripped flow relative to the untripped transitional flow regime, resulting in net cylinder lift coefficient being halved to $C_L = 1.8$ from $C_L = 3.6$. The remaining part of the paper examines the flow differences that lead to such a drastic change in the jets' interaction with the flow. First, Figure 17 shows the time-averaged radial pressure gradient field generated by the 3-D jets at $\alpha = 125°$ and $C_\mu^F = 0.095$ without tripping and with the $\theta = 60°$ trip. Average pressure gradients were calculated from the Reynolds Averaged Navier Stokes relations assuming spanwise flow symmetry about the PIV plane, which is located at the spanwise center of one of the 3-D sweeping jets. On the untripped cylinder (Figure 17a), the regions within 0.08*D* from the surface upstream of the jets, where the jets' location is marked by a triangle, and 0.16*D* from the surface downstream of the jets have a negative radial pressure gradient, while the flow farther from the surface generally exhibits a positive radial pressure gradient, indicating a pressure decrease towards the boundary layer along the convex surface upstream of the active jet, assisting the flow attachment. Thus, a distinct region of positive radial pressure gradient appears above the surface upstream of the jets from $\theta = 114°$ to 126° corresponding to the attached boundary layer accelerating over the backwards facing slope and step geometry directly upstream of the jets. Because the planar PIV is located at the spanwise center of one of the 3-D fluidically oscillating actuators, the sweeping jet issued only crosses the

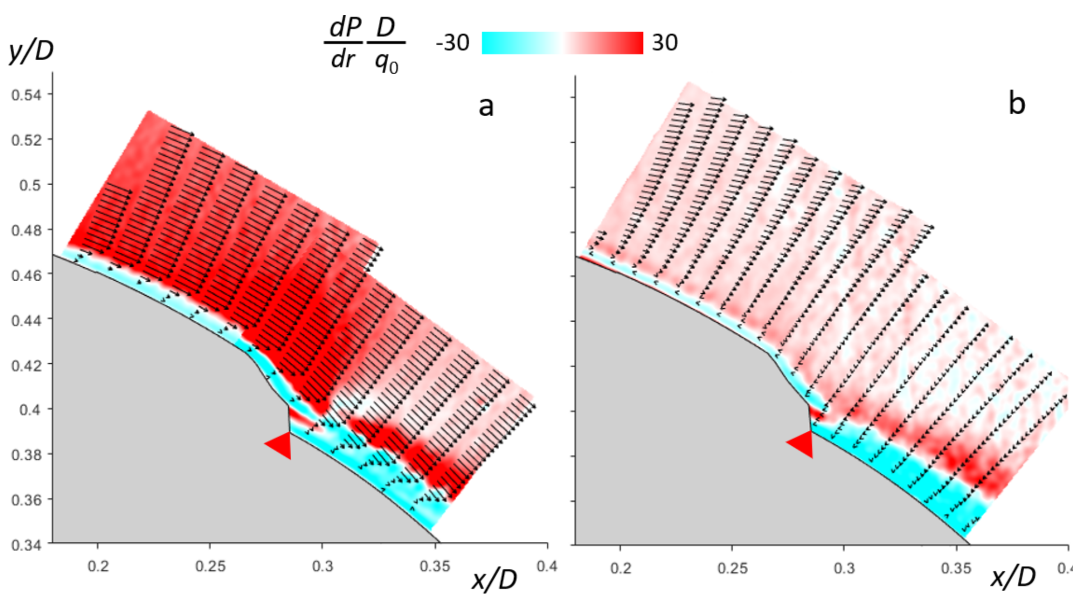

Figure 17. *Time averaged flow fields normal to span and color contours of normalized radial pressure gradient with 3-D jets at* $\alpha = 125°$ *and* $C_\mu^F = 0.095$ *on the untripped cylinder (a) and cylinder with* $\theta = 60°$ *trip (b).*

measurement plane in a small fraction of the captured instantaneous flow field realizations. Therefore, the time-averaged pressure gradient field only registers the core of the sweeping 3-D jet from the jet orifice to $0.15D$ downstream, with this core developing a positive radial pressure gradient above it and a negative one below it. Downstream of the jet there are complex interactions between adjacent 3-D jets sweeping spanwise at random phases with respect to each other (an example of this is shown by the high surface TKE region in Figure 12f), and these interactions entrain the outer flow (Rackers et al., 2025). Here, these interactions appear in a $0.16D$ thick layer of negative radial pressure gradient on the surface and a $0.15D$ thick layer of positive radial pressure gradient directly above that, entraining flow into the boundary layer.

The average radial pressure gradient field above the tripped cylinder with the same actuation of C_μ^F = 0.095 at α = 125° (Figure 17b), also exhibits a layer of negative pressure gradient on the surface ($0.06D$ thick upstream of the jets and $0.16D$ thick downstream). Because the trip causes the flow to separate in the region shown for a large fraction of the instantaneous realizations, the distinct region of positive radial pressure gradient in Figure 17a above the surface from θ = 114° to 126° is absent in Figure 17b. However, even as the 3-D jets issue primarily into the separated wake, the core of the local sweeping jet still produces the negative radial pressure gradient beneath it and the positive one above it from the jet orifice to $0.17D$ downstream. The actuation also still produces the $0.16D$ thick layer of negative radial pressure gradient on the surface downstream of the jets and the $0.15D$ thick layer of positive radial pressure gradient directly above that, though the positive pressure gradient in the outer layer is less intense in the mainly separated flow. The fact that with tripping upstream, the 3-D jets produce a similar average pressure gradient field downstream of actuation to that of the 3-D jets with no tripping upstream indicates that the local Coanda effect of the jets is not eliminated by the θ = 60° trip, and flow is still on average entrained into the jets. This agrees with the discussion in Figure 14d, where the jets are shown to fluctuate in lift generation and occasionally produce an unstable equilibrium of separation suppression like in the untripped case.

Further insight into the effect of the trip on the noted drop in the effected lift when the upstream flow is tripped at θ = 60° and the 3-D jets are active at α = 125° (C_μ^F = 0.095) is sought through Proper Orthogonal Decomposition (POD) of the instantaneous velocity fields over the PIV-measured 500 flow field realizations, collected both the upstream and downstream of the cylinder apex, and both for the controlled and uncontrolled flow. After initial decomposition, the 50 modes with the highest energy contributions were utilized to reconstruct instantaneous structures in the boundary layer and near flow, essentially utilizing the POD analysis for a lowpass filter. Some characteristic instantaneous flow fields are shown in Figure 18. The upstream view of the tripped flow (Figure 18a) indicates a typical boundary layer flow close to the surface, being slightly displaced and smoothly reconnecting with the surface past the trip, which is partially seen in the view. However, once this flow encounters an adverse pressure gradient and reaches the separation point, the view of which is shown in Figure 18b, a clear shedding of organized small-scale vortices is noted in instantaneous flow fields. Since these vortices are not formed within a shear layer past separation, but are rather convected through the boundary layer, it is argued that the small perturbations induced by the upstream trip (of height t/D = 0.0013 in a $0.01D$ thick boundary layer), although not detectable is the upstream measurements, begin to be amplified once the boundary layer encounters adverse pressure gradient. The trip may modulate perturbations in the boundary layer via the intermittent formation of a laminar separation bubble behind it, a phenomenon observed in numerical simulations by Chopra and Mittal of a circular cylinder in transitional flow

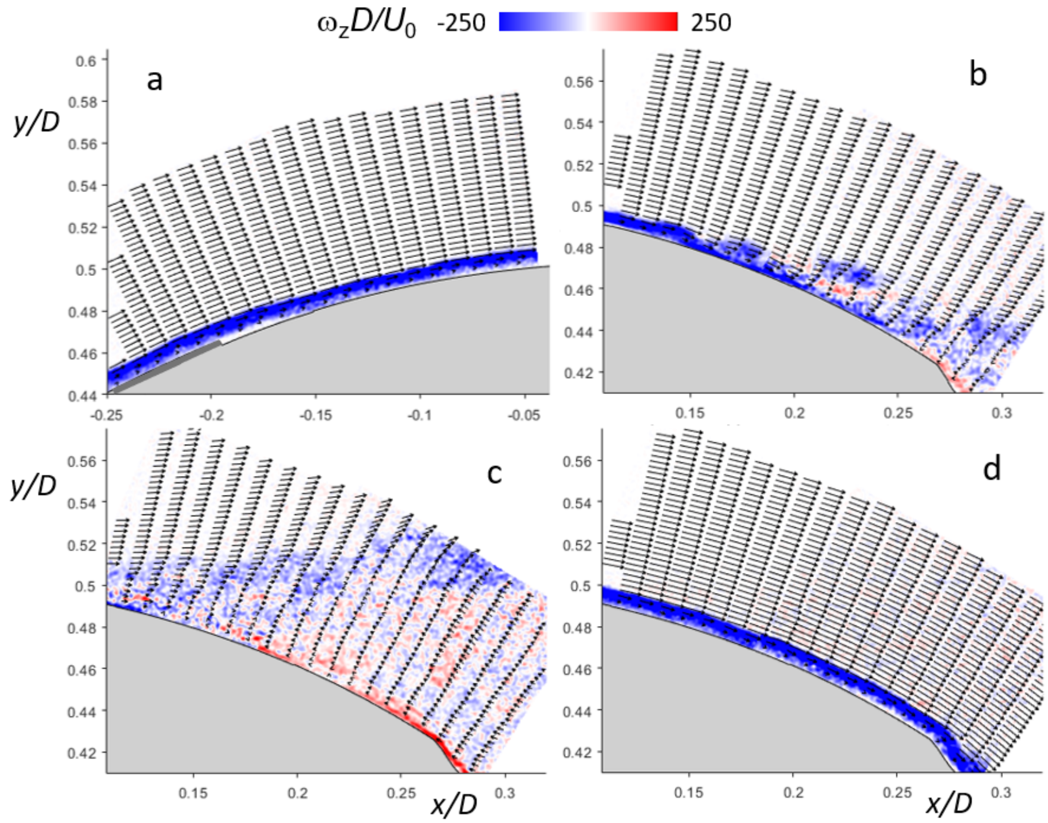

Figure 18. POD-reconstructed instantaneous flow fields normal to span and color contours of normalized spanwise vorticity for the cylinder with θ = 60° trip. Upstream and downstream views of unactuated flow (a, b). Downstream views of actuated flow at C_μ^F = 0.095, including a select separated instant (c) and a select attached instant (d).

with a trip of height $t/D = 0.01$ (2022, $Re_D = 1\cdot10^5$). It is also noted that just prior to flow separation, the coherent vorticity perturbations seen in Figure 18b have an average wavelength of ~0.06D averaged across the POD-reconstructed instantaneous flow field realizations and are convected at a speed of ~0.44U_0, such that the estimated average perturbation frequency on the surface is ~1 kHz, which is on the order of the measured oscillation frequency of the fluidically sweeping 3-D jets at 3-4 kHz. This similarity in frequency may point to a coupling between the jets' oscillations and trip-generated perturbations in the attached boundary layer that disturbs the 3-D jet's steady suppression of separation. As stated above, the controlled flow in any instance of time may be either attached or separated due to the unsteady nature of its attachment. Figures 18c and d further illustrate this with a representative separated POD-reconstructed instant and a representative attached one. However, in the presented actuated flow, these two realizations are not equally probable and the most commonly observed instantaneous flow condition is the one shown in Figure 18c, with separation occuring at θ = 110°. The instant in Figure 18d represents the rare instance of fully attached flow, which were observed to occur simultaneously with measured instantaneous lifts of $C_L \approx 3.6$ (see the small probability distribution peak in Figure 14d inset). Various intermediate states of attachment are also found in the instantaneous flow realizations. The observed cycle of separation and reattachment in the instantaneous flow field data agrees with an average lift reduction mechanism whereby the 3-D jets attach the outer flow similarly to in the untripped case but, it can be argued, the subsequent loss of attachment may be resulting from intermittent boundary layer perturbations produced at the upstream trip, propagated to the actuators, and interacting with the acting flow control over the jet orifice lip. The resulting time-averaged lift generation is thereby significantly reduced from the untripped case. However, if the 3-D jets are moved sufficiently upstream or the level of actuation is sufficiently increased, the perturbations from the trip may be no longer of sufficient strength to interrupt the steady suppression of separation by the 3-D jets (cf. Figure 13d, e).

To further investigate the perturbance generation and growth past the trip, the radial velocity component of the baseline tripped flow over three separate measurement windows is decomposed by POD and the highest energy modes in each window are shown in Figure 19. In the view just downstream from the trip and upstream from the apex, even the highest energy mode is not clearly organized and it is confined to a rather thin boundary layer. In addition, this mode contributes to only about 0.8% of the total energy, which is another indication of the lack of coherence. Further downstream in the adverse pressure gradient (Figure 19b), the highest energy-contributing modes consist of regular concentrations of radial velocity of alternating sign. The prominence of this periodic structure in the radial velocity modes captures the rolling behavior of the amplified perturbations observed in the instantaneous flow fields, where the flow within the front of the perturbations is observed in the POD-reconstructed instants to be biased towards the surface and the flow within the trailing side of the perturbations is observed to be biased away from the surface (not shown). Despite being the first boundary-layer mode, the mode in Figure 19b is also not of exceptionaly high energy but represents about 5.6% of the total captured energy, indicating that to capture the encompasing BL dynamics, many more modes need to be retained. The first boundary layer mode in the POD decomposition just upstream from the jet (Figure 19c) represents 2.3% of the total captured energy and exhibits similar regular concentrations of radial velocity of alternating sign along the surface as the ones in Figure 19b, but growing spatially with the boundary layer and into the incipient flow separation.

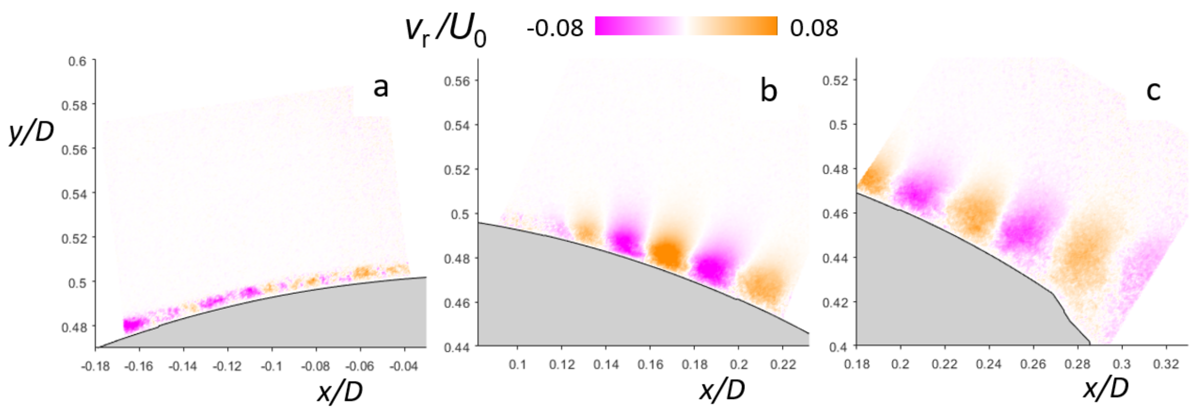

__Figure 19.__ Color contours of the radial velocity POD boundary layer modes of highest energy contribution on the baseline tripped cylinder; views at three azimuthal locations on the surface of the cylinder from the windward to the leeward side (a, b, c).

V. CONCLUSIONS

Motivation for the present study comes from circulation control approaches on a rotorcraft cylinder boom that have been used to effect counter torque to replace the conventional tail rotor in NOTAR configurations. These loads that have been traditionally realized by the Coanda effect of a 2-D steady wall jet in the rotor downwash. The present experimental investigation explores utilization of both 2- and 3-D Coanda wall jets for lift production and drag reduction on a circular cylinder in the transitional flow regime (Re = 2.1×10^5). In particular, the effected aerodynamic loads on a cylinder are investigated relative to the azimuthal orientation of a spanwise array of jets, where each array was composed of five equal spanwise segments across the wind tunnel span carrying either discrete fluidically oscillating jets (3-D configuration) or a single slit-orifice (2-D configuration). In addition, differences in controlling the tripped flow, which is a usual approach for bypassing the transitional flow regime, are assessed for the 3-D flow control array. The global flow characterization was done by aerodynamic load measurements, whereas the local flow features about the upper cylinder surface were characterized by spanwise-normal planar PIV measurements on the surface at 60° ≤ θ ≤ 145° and azimuthal static pressure profiles at fixed spanwise position of the cylinder.

Besides the difference in discretely distributed flow control elements of the fluidic-oscillating jets and pseudo-2-D continuous slot-jets (split across five control modules), the main difference between the two flow control approaches was driven by the about five-times larger total orifice area of the 2-D jet. Hence, the 2-D jet requires a significantly higher actuation mass flow rate coefficient C_{Q} to attain the same force-momentum coefficient C_μ^F. Interestingly, this disbalance is also reflected in the higher inlet power coefficient C_{IP}, defined from the power needed for an ideal compressor to continuously bring a quiescent, ambient air supply to the measured conditions at the inlet of the model's spar outside the wind tunnel during actuation. At the maximum tested actuation mass flow rate of C_{Q} = 0.010, the 3-D jets effect C_μ^F = 0.15, inducing a maximum lift of C_{L} = 4.5, over 3 times greater than that induced by the 2-D jet (C_{L} = 1.3) with the same actuation mass flow (and smaller C_μ^F = 0.032). In addition, at an equivalent actuation momentum coefficient $C_\mu^F \approx 0.032$, the 2-D jet generated comparable but somewhat lower lift than the 3-D jets for the actuation angles up to the critical angle for the 2-D jet of α_{crit} = 100° when the 2-D jets begin to lose their effectiveness. Past their critical angle, performance of the 2-D jets precipitously drops while the 3-D jets continue to increase lift coefficient up to C_{L} = 2.0 at their critical angle α_{crit} = 120°, after which their effectiveness also diminishes. The extended azimuthal range of effectiveness of the 3-D jets is attributed to their localized strong momentum influx compared to the much weaker local effect of the 2-D jets for an equal total C_μ^F. It is noteworthy that whenever control jets impart a net increase in lift, it is also associated with the drag reduction of about 40%.

As the experiments were performed at a transitional Reynolds number (Re_{D} = 2.1·10^5), the effects of tripping the flow upstream of the 3-D jets were explored as well. A small trip of the height t/D = 0.0013 was placed at θ = 60°. For actuator jet positions far upstream of α_{crit} for a given C_μ^F, BL tripping does not significantly alter the lift generation or drag reduction effected by the 3-D jets. However, when the jets are positioned near α_{crit} and past that azimuthal orientation, a progressive loss of lift generation was measured relative to the untripped transitional flow. It was found that small perturbations imposed by the trip that cannot be resolved within the upstream boundary layer get amplified once the boundary layer is in the adverse pressure gradient. It can be argued that such transitional vortical structures, growing spatially, likely interfere with the control jets as they traverse the jet orifice lip, resulting in the unsteady nature of the controlled flow attachment, also reflected in a wide distribution of instantaneous lift coefficients associated with this control state.

Acknowledgment/Disclaimer

This work was sponsored by the Army Research Office (ARO), under grant number W911NF2220180. The views and conclusions contained herein are those of the authors only and should not be interpreted as representing those of ARO, the U.S. Army, or the U.S. Government.

REFERENCES

Achenbach, E, and Heinecke, E., "On Vortex Shedding from Smooth and Rough Cylinders in the Range of Reynolds Numbers $6 \cdot 10^3$ to $5 \cdot 10^6$," *Journal of Fluid Mechanics*, Vol. 109, pp. 239-251, August 1981. https://doi.org/10.1017/S002211208100102X

Bearman, P. W., "On vortex shedding from a circular cylinder in the critical Reynolds number régime," *Journal of Fluid Mechanics*, Vol. 37, No. 3, pp. 577-585, July 1969. https://doi.org/10.1017/S0022112069000735

Chopra, G. and Mittal, S., "The Effect of Trip Wire on Transition of Boundary Layer on a Cylinder," *Physics of Fluids*, Vol. 34: 054103, 2022.

Dionisio, F. A. and Nurick, A., "Investigation of a Circulation Controlled Cylinder using an Adaptive Wall Wind Tunnel," *J. Aircraft*, Vol. 38, No. 3, pp. 521-527, May 2001. https://doi.org/10.2514/2.2792

Dunham, J., "A Theory of Circulation Control by Slot-Blowing, Applied to a Circular Cylinder," *J. Fluid Mechanics,* Vol. 33, No. 3, pp. 495-514, September 1968. https://doi.org/10.1017/S0022112068001473

Ekmekci, A. and Rockwell, D., "Effects of a Geometrical Surface Disturbance on Flow Past a Circular Cylinder: A Large-scale Spanwise Wire," *Journal of Fluid Mechanics*, Vol. 665, 2010, pp. 120-157.

Englar, R., "Circulation Control Pneumatic Aerodynamics: Blown Force and Moment Augmentation and Modification; Past, Present and Future," AIAA 2000-2541, June 2000. https://doi.org/10.2514/6.2000-2541

Englar, R., Blaylock, G., Gaeta, R., Jones, G., Milholen, W., "Recent Experimental Development of Circulation Control Airfoils and Pneumatic Powered-Lift Systems," AIAA 2010-345, January 2010. https://doi.org/10.2514/6.2010-345

Ghee, T. A. and Leishman, J. G., "Unsteady Circulation Control Aerodynamics of a Circular Cylinder with Periodic Jet Blowing," *AIAA J.*, Vol. 30, No. 2, pp. 289-299, February 1992. https://doi.org/10.2514/3.10916

Hanvey, S., "NOTAR – No Tail Rotor (Circulation Control Tail Boom)," Presented in *Report to the Aerospace Profession – Proceedings of the 26th Symposium*, pp. 308-332, 1982.

Higuchi, H., Kim, H.J. and Farell, C., "On Flow Separation and Reattachment Around a Circular Cylinder at Critical Reynolds Numbers," *Journal of Fluid Mechanics*, Vol. 200, 1989, pp. 149-171.

Hoerner, S., *Fluid-Dynamic Drag: Practical Information on Aerodynamic Drag and Hydrodynamic Resistance*, Hoerner Fluid Dynamics: Bakersfield, CA, 1965.

Igarashi, T., "Effect of Tripping Wires on the Flow Around a Circular Cylinder Normal to an Airstream," *Bulletin of JSME*, Vol. 29, 1986, pp. 2917-2924.

Jones, G. S., and R. J. Englar, "Advances in Pneumatic-Controlled High-Lift Systems Through Pulsed Blowing", AIAA 2003-3411, June 2003. https://ntrs.nasa.gov/archive/nasa/casi.ntrs.nasa.gov/20030062153.pdf

Klemin, A., "The Problem of the Helicopter," *The Scientific Monthly*, Vol. 67, No. 2, pp. 127-130, August 1948. https://www.jstor.org/stable/22321

Levinsky, E. S. and Yeh, T. T., "Analytical and Experimental Investigation of Circulation Control by Means of a Turbulent Coanda Jet," NASA CR-2114, September 1972. https://ntrs.nasa.gov/api/citations/19720023364/downloads/19720023364.pdf

Lockwood, V., "Lift Generation on a Circular Cylinder by Tangential Blowing from Surface Slots," NASA TN D-244, May 1960. http://catalog.hathitrust.org/api/volumes/oclc/73507654.html

Logan, A. and Kumar, K., "NOTAR Helicopter – A New Approach to Helicopters," Presented at Society of Allied Weight Engineers 45th annual conference, Williamsburg, Virginia, USA, May 1986. https://www.sawe.org/papers/1734

Luo, X., Zhang, C. and Wang, H., "Experimental Study of No Tail Rotor (NOTAR) Helicopter," Presented at ICAS 2000 Congress, Harrogate, UK, August 2000. https://www.icas.org/ICAS_ARCHIVE/ICAS2000/PAPERS/ICA0181.PDF

McDaniel, R., "Jet Thrust as a Counter-Torque Force for Single-Rotor, Shaft-Powered Helicopters," Ph.D. Dissertation, Georgia Institute of Technology, June 1961.

Metral, A.R., On the phenomenon of fluid veins and their applications, the Coanda effect, AF Translation, F-TS-786-RE, 1939.

Neuendorf, R. and Wygnanski, I., "On a Turbulent Wall Jet Flowing over a Circular Cylinder," *J. Fluid Mechanics,* Vol. 381, pp. 1-25, February 1999. https://doi.org/10.1017/S0022112098003668

Neuendorf, R., Lourenco, L. and Wygnanski, I., "On Large Streamwise Structures in a Wall Jet Flowing over a Circular Cylinder," *Physics of Fluids*, Vol. 16, No. 7, pp. 2158-2169, July 2004. https://doi.org/10.1063/1.1703531

Newman, B. G., "The Deflexion of Plane Jets by Adjacent Boundaries – Coanda Effect," in *Boundary Layer and Flow Control: Its Principles and Applications, Volume 1*, Pergamon Press, edited by G. V. Lachmann, pp. 232-264, 1961.

Nurick, A., "Experimental Investigation of a Helicopter Circulation-Controlled Tail Boom," *J. Aircraft,* Vol. 38, No. 3, pp. 528-535, May 2001. https://doi.org/10.2514/2.2793

Oh, S. and Roberts, L., "Control of Separated Flow Past a Cylinder using Tangential Wall Jet Blowing," NASA CR-185918, July 1989. https://ntrs.nasa.gov/api/citations/19890019955/downloads/19890019955.pdf

Rackers, N., DeSalvo, M., Vukasinovic, B. and Glezer, A., "Circulation Control Over a Circular Cylinder by a Spanwise Array of 3D Coanda Wall Jets," AIAA 2025-1681, January 2025. https://doi.org/10.2514/6.2025-1681

Runge, W., Buysschaert, F., Hayez, J., Carlier, F., Antoine, H., Hendrick, P., Dimitriadis, G. and Degrez, G., "Numerical and Experimental Investigation of Slot-Blown Air over a Cylinder," *Progress in Flight Physics*, Vol. 7, pp. 229-244, June 2015. https://doi.org/10.1051/eucass/201507229

Szepessy, S., and Bearman, P. W., "Aspect ratio and end plate effects on vortex shedding from a circular cylinder," *Journal of Fluid Mechanics,* Vol. 234, pp. 191-217, January 1992. https://doi.org/10.1017/S0022112092000752

Sampatacos, E., Morger, K. and Logan, A., "NOTAR: The Viable Alternative to a Tail Rotor," AIAA 1983-2527, October 1983. https://doi.org/10.2514/6.1983-2527

Schewe, G., "Reynolds-number Effects in Flow Around More-or-less Bluff Bodies," *Journal of Wind Engineering and Industrial Aerodynamics*, Vol. 89, 2001, pp. 1267-1289.

Shih, W., Wang, C., Coles, D. and Roshko, A., "Experiments on Flow Past Rough Circular Cylinders at Large Reynolds Numbers," *Journal of Wind Engineering and Industrial Aerodynamics*, Vol. 49, No. 1-3, pp. 351-368, December 1993. https://doi.org/10.1016/0167-6105(93)90030-R

Sikorsky, I., "Technical Development of the VS-300 Helicopter during 1941," *Journal of the Aeronautical Sciences*, Vol. 9, No. 8, pp. 309-311, June 1942. https://doi.org/10.2514/8.10892

Vukasinovic, B., Funk, R. and Glezer, A., "Circulation Control Using Arrays of Fluidically Oscillating Jets," *AIAA Journal*, Vol. 63, No. 10, pp. 4023-4034, October 2025. https://doi.org/10.2514/1.J064722

Williams, J. and Cummings, R., "Experimental Investigation of a Circular Cylinder under the Effects of Tangential Slot Blowing," AIAA 1996-2435, June 1996. https://doi.org/10.2514/6.1996-2435

Zdravkovich, M. M., "Conceptual Overview of Laminar and Turbulent Flows Past Smooth and Rough Circular Cylinders," *Journal of Wind Engineering and Industrial Aerodynamics*, Vol. 33, No. 1-2, pp. 53-62, March 1990. https://doi.org/10.1016/0167-6105(90)90020-D